LUND UNIVERSITY

DIVISION OF PARTICLE PHYSICS

Investigating R_T using two-particle angular correlations in proton-proton collisions

Bachelor thesis by:
Dilan Chroscik

Supervised by:
Alice Ohlson
David Silvermyr

Date:
August 11, 2020

Abstract

The observable, R_T, is investigated using two-dimensional ($\Delta\eta$, $\Delta\varphi$) angular correlations, where $\Delta\eta$ and $\Delta\varphi$ are the differences in pseudorapidity and azimuthal angle respectively, between the trigger and associated tracks. The analysed data consists of reconstructed tracks, from proton-proton collisions at collision energy $\sqrt{s} = 13$ TeV, taken from the ALICE detector at the LHC. Correlations are constructed in three configurations, where the selection of trigger and associated tracks is changed. Analysis of the correlations imply that R_T has high sensitivity to the underlying event, as well as a tendency to select event shapes with dominating back-to-back jet fragmentation for low R_T. A disappearance of the away-side peak in $\Delta\varphi$-projections is observed in high R_T events. We also see significant near-side correlations in all configurations, even within the transverse region.

Contents

1 Introduction

The Large Hadron Collider (LHC) provides the possibility to study matter at high temperatures and energy densities, where the Quark-Gluon Plasma (QGP) is expected to be formed [1]. The QGP is formed at the extreme pressure and temperate limits of Quantum Chromodynamics (QCD). From QCD we get two main concepts: *color confinement* which tells us that quarks and gluons usually are confined in hadrons due to their color charge, and *asymptotic freedom* which describes how the strong force experienced between color-charge carrying particles increases with increasing distance, while decreasing with decreasing distance. Therefore, the constituents of a hadron appear to be free when in close proximity of each other, and are pulled back in if the distance increases between them. However, a QGP is a state of matter where the quarks and gluons become deconfined and interact quasi-freely with other quarks and gluons.

In heavy ion collisions at the LHC, enough energy density is provided to create a QGP with a very short lifetime. There are several proposed signatures of QGP creation, such as long range angular correlations which arise from the collective expansion of the created medium. These long range correlations are usually referred to as the *ridge structures*. The ridge has been observed in heavy ion collisions, and is understood to be a consequence of the translation of initial positions-space anisotropy into final momentum-space anisotropy. However, recently the ridge has been observed in proton-proton collisions as well [2][3], which was a surprise since the initial nuclear matter density in proton-proton collisions is not thought to be enough for QGP creation.

In high energy particle physics, different observables are used to categorize the collision events in order to analyze them. The relative transverse activity, R_T, has been proposed to be used as a tool to select events in the search for signs of QGP in proton-proton collisions. However, the event shape selection of R_T is not yet fully understood. The goal of this study is to investigate R_T using two-particle angular correlations, in order to understand how this observable selects event topologies to fully utilize this observable as a categorization tool.

2 The Standard Model

The standard model (Fig. 1) is a theory in particle physics which tries to describe the interactions between all three types of fundamental particles known in nature. The three types of fundamental particles being *leptons*, *quarks* and *bosons*. Leptons and quarks are both *fermions* with half-integer spin, whilst the force-carrying gauge bosons have spin-1 and the Higgs boson has spin-0. The fermions are divided into three *generations*, higher generation fermions have higher mass and are more unstable. Types of quarks within these generations are called *flavours*. There are a total of six flavours: *up, down, charm, strange, top* and *bottom*. There are also six types of leptons. These leptons are divided into two groups: charged and neutral. Charged leptons include: *electrons, muons* and the *tau*, while the neutral leptons, also known as *neutrinos*, include: *electron-neutrino, muon-neutrino* and *tau-neutrino*. [4]

There are four gauge bosons that mediate three of the four forces, so far no gauge boson for the gravitational force has been observed. The *photon* mediates the electromagnetic force, described by Quantum Electrodynamics (QED), and interacts with particles carrying electric charge. The *gluon* mediates the strong force, described by QCD, and interacts with particles carrying color charge. Unlike the photon, the gluon carries the charge it mediates and can therefore self-interact. The Z and W-bosons mediate the weak force and interact with all quarks and leptons. [5]

Due to the color charges of the quarks, they usually combine in either groups of two ($q\bar{q}$) or three (qqq or $\bar{q}\bar{q}\bar{q}$) in order to create a color neutral composition. These color neutral states are called *hadrons*. Quarks and gluons are collectively known as *partons*. All particles have an associated anti-particle, where the charge is opposite of the original particle [4]. These charges include electric and color charges.
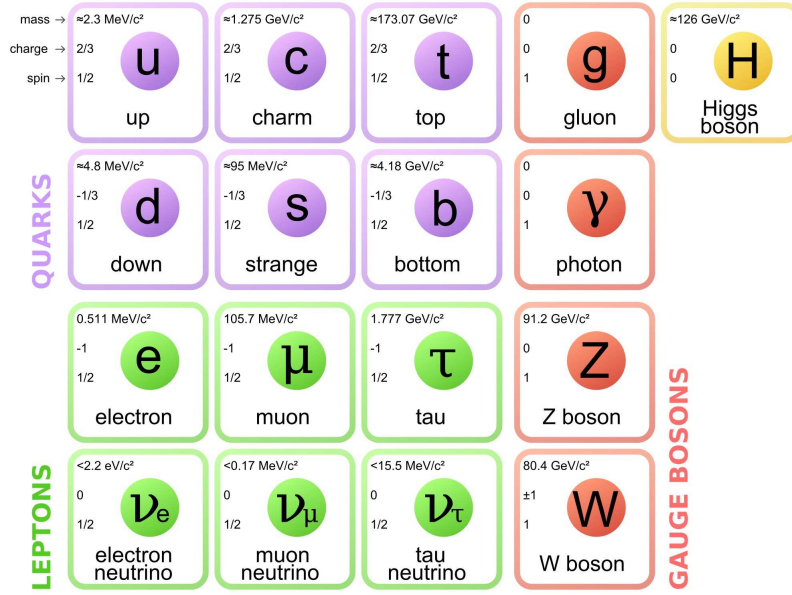
Figure 1: The standard model with all three generations of *quarks* and *leptons*, as well as the *gauge bosons* and the *Higgs boson*. [6]

3 Quantum Chromodynamics

QCD describes the interaction between particles carrying color charge, i.e. quarks and gluons. Many analogies can be made between QCD and QED, however as previously mentioned, the gluon carries color charge which make the interactions more complicated than QED interactions with photons that carry no charge. From QCD we get two important concepts, *color confinement* and *asymptotic freedom*.

Color confinement describes how only color neutral particles can be observed [4]. There are three color charges (*red*, *green* and *blue*) and three anti color charges (*anti-red*, *anti-green* and *anti-blue*). To make a color neutral particle, quarks with all three colors (baryons) or quarks with a color and an anti-color (mesons) must bind into a hadron.

The strong force, which acts on the quarks, is relatively weak at close proximity. This gives the quarks within a hadron a bit of freedom to move, this is called asymptotic freedom [5]. However, the strong force becomes stronger with increasing distance unlike the other forces like gravity or electromagnetism. As a consequence of the self-interacting gluon, the *field lines* of the strong force are more like tubes and are very directional, unlike the electric field lines which permeate all of space. The consequence of this is that trying to separate two quarks takes more energy than to create a quark anti-quark pair. As the quark is being pulled further and further away from the other quark, the tubes of color force break and new pairs are formed (Fig. 2).
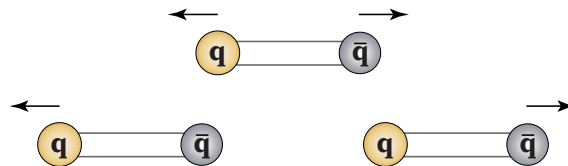
Figure 2: A depiction of a quark anti-quark pair being separated and forced to create a new quark anti-quark pair, due to the strength of the strong force increasing with increased distance. The colors in the figure are not to be confused with the color charges of the quarks.

This can lead to a chain reaction which produces quark pairs, which in turn can form hadrons. These particles will generally go in the same direction as the initial quark, causing charged tracks and clusters of energy deposits to appear in our detectors. The collection of hadrons travelling in the same general direction, resulting from the hard (high momentum transfer) scattering partons, is often called a *jet*.

4 Proton-proton collisions

In proton-proton hard scattering events, quarks from the colliding protons scatter with high transverse momentum. The outgoing quarks undergo hadronization due to color confinement from QCD, which leads to jet formation. Most collisions result in 2-to-2 scattering, where two incoming quarks scatter out to two outgoing jets (Fig. 3). The underlying event (UE) consists of the remaining partons from the protons as well as the initial and final-state radiation.
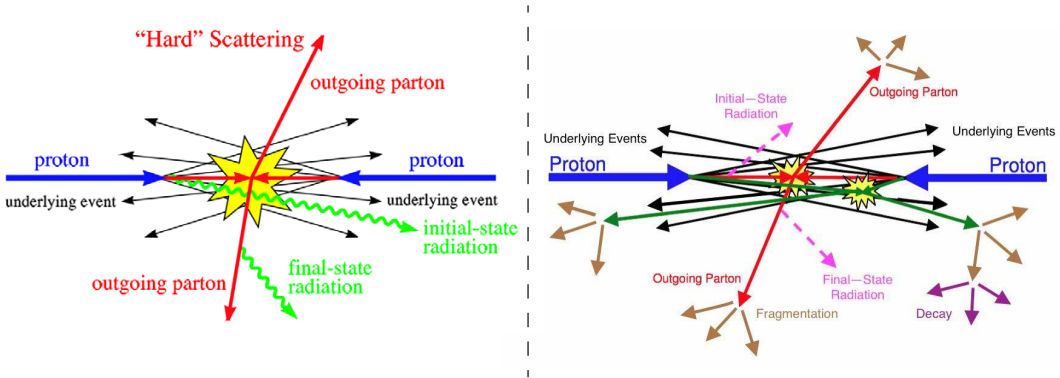

Figure 3: Proton-proton collisions resulting in hard 2-to-2 scattering, with high transverse momentum (p_T) transfer. The initial and final state radiation is indicated in the left figure [7]. In the right figure [8] we see an UE due to multiple parton scattering.

Due to conservation of momentum, the jets created in these collisions tend to go back-to-back. Therefore, the region transverse to the jet axis may be where we can best study the UE [9]. The right side of Fig. 3 shows an underlying event from soft scattering arising from multiple parton interaction. As R_T (defined in section 9) measures the relative transverse activity, it is believed to be able to distinguish between events with small and large UE, and could therefore be used to probe this multiple parton interaction [10].

5 Quark-Gluon Plasma

At high energy densities, partons become deconfined. This forms a new state of matter called Quark Gluon Plasma (QGP), where the partons are free and strongly interacting outside their original hadrons. The QGP exhibits collective behavior similar to a fluid described by hydrodynamics [12].

Some models indicate that in the early universe, shortly after the Big Bang, most matter was in this QGP state due to the high energy densities [4]. However, it is also possible to create QGP in heavy ion collisions. This is done at the LHC with lead ions. The lifetime of the QGP produced is however very short, around 10^{-23} seconds. It is therefore hard to study directly. Instead, one searches for signatures of QGP creation. One such signature is jet quenching, where jets traveling through the medium lose some of their momenta to the medium and particle production becomes suppressed. Another signature of QGP creation is bulk particle creation, due to hadronization of the cooling medium.

6 Heavy ion collisions

Heavy ions consist of many individual protons and neutrons and since not all collisions are head-on, some nucleons do not interact in the collision. The protons and neutrons that do interact in the collision are called *participants*, while the non-interacting ones are called *spectators*.
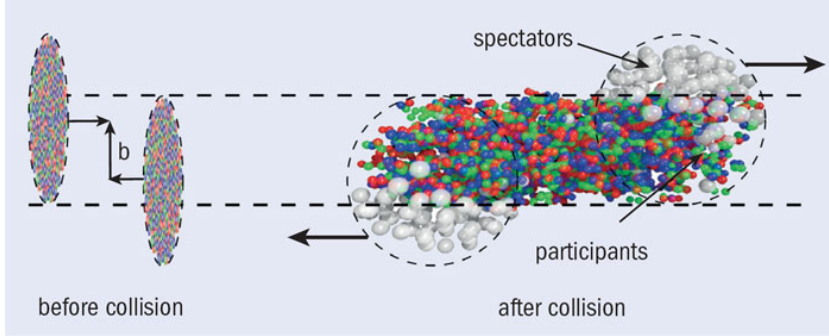

Figure 4: Left: Before a heavy ion collision. The centers of the ions are separated by a distance equal to the magnitude of the impact parameter, b. Right: After the collision. The spectators continue without interacting in the collision, while the participants interact. [11]

The impact parameter b (Fig. 4) is the distance between the centers of the colliding ions, however, it can not be measured directly. Instead one measures *centrality* which is dependent on the impact parameter b. A head-on collision, with small b, is characterized by a high centrality and yields a higher particle production, while a glancing collision, with large b, has a small overlap and low centrality.

As the heavy ions collide, the participants can scatter. In hard scattering, the colliding partons have high momenta transfer and will produce hadrons and jets. While, in soft scattering, the colliding partons do not have large momenta which leads to multiple soft scattering that produce gluons and quark-antiquark pairs. The produced partons which do not bind with others into new hadrons are effectively free and interact with the other free partons, in what can be described as a medium. Once the medium thermalizes it reaches a phase transition into QGP and can be described hydrodynamically. As the QGP undergoes hydrodynamic expansion, often called an expanding fireball, the medium cools down due to decreasing energy densities. When the densities become too low to maintain the QGP state, the partons start to hadronize in what is called the *freeze-out*. [5]

6.1 Collective flow

In order for the QGP to behave hydrodynamically it needs to thermalize to gain the properties of a fluid. As these properties are gained and the medium expands, the particles inside the medium can not be completely described as free point particles in a gas, since their behavior is governed by the mediums collective expansion. This collective behavior in heavy ion collisions can be described by the *collective flow*, which is sensitive to the early evolution of the expansion. [12]

The collision centrality, as well as the collision geometry, affect what type of flow will be observed. The most central collisions are head-on and symmetric collisions between two flat discs, which only yields the azimuthally symmetric *radial flow*. Peripheral collisions have an initial position-space anisotropy which yield various types of *anisotropic flow* depending on the geometry of the initial spatial anisotropy [12]. The interacting area of central and peripheral collisions are depicted in Fig. 5, where the characteristic anisotropic almond shape responsible for the *elliptic flow* (defined below) can be seen in the non-central collisions. These are of course approximations since the ions are not perfect spheres or discs, they are made of individual particles which are not static.
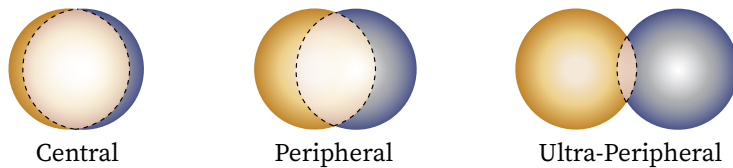
4

Figure 5: Central and peripheral heavy ion collision. The peripheral collisions are anisotropic in position space, seen as almond shapes in the interaction area.

A peripheral collision can be seen in Fig. 6, where the reaction plane, for which the flow is azimuthally symmetric around, is indicated by Ψ_2 in the x-y-plane (transverse plane). The ions depicted are travelling in opposite directions in the z-axis, which is the beam-axis. The symmetry around the reaction plane arises from pressure gradients, created due to collective behavior and the initial position space anisotropy, which are causing the medium to expand preferentially in the direction of the reaction plane. A Fourier expansion of an event with N particles, with respect to the reaction plane, can be used to describe the final azimuthal momentum distribution [12]:

$$E\frac{d^3N}{d^3p} = \frac{d^2N}{2\pi p_T dp_T dy}\left[1 + \sum_{n=1}^{\infty} 2v_n \cos\left(n(\varphi - \Psi_n)\right)\right] \tag{1}$$

where p is the total momenta and p_T is the part of the momenta in the transverse plane respectively (defined in Section 8.1). The y denotes the y-axis in the transverse plane and φ denotes the azimuthal angle of the particle. The Fourier (or flow) coefficient of the nth harmonic is given by v_n and the reaction plane of the nth harmonic by Ψ_n.

All harmonics correspond to different types of the collective flow, where the lowest-order harmonic, v_0 is the only one without anisotropy in the inital position space. The higher order coefficients are associated with anisotropic flow of nth order. In Fig. 6 the initial geometry of the collision indicate that there will be a resulting anisotropy in the final momentum space corresponding to the second harmonic, called elliptic flow due to the almond like shape. The third harmonic is called triangular flow, due to the initial collision geometry resembling a triangle.
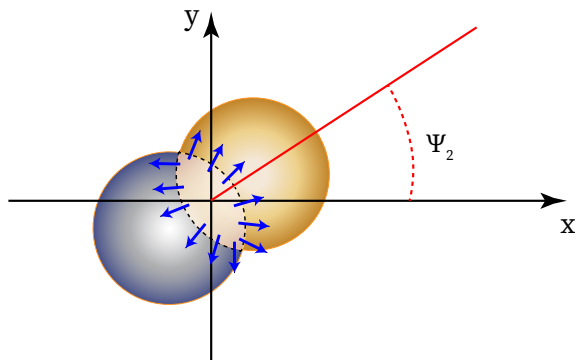

Figure 6: A heavy ion collision, in the x-y-plane, with the reaction plane indicated by Ψ_2. Pressure gradients cause a final anisotropic flow to be symmetric around the reaction plane.

6.2 The ridge structure

The long range correlation (Fig. 7) in pseudorapidity $\Delta\eta$, which is localized in $\Delta\varphi$, has been shown to be well described by the first three components of the Fourier expansion: directed flow, elliptic flow and triangular flow. Observations indicate that triangular flow has a large contribution to this effect, particularly in central collisions, where $v_2 \approx v_3$ [13].

The ridge structure has been observed in proton-proton collisions as well, which was not expected in the community. It was assumed that the number of participants is too low in proton-proton collisions to yield a significant area of spatial anisotropy, which in turn can lead to anisotropic flow. The proton-proton collisions were expected to be simple baselines with predominantly standard QCD effects.

As a consequence, one of the efforts in the heavy-ion physics community is to find a way to classify and select proton-proton collisions which display QGP-like features. One such classification observable is R_T (defined in section 9), which has been proposed as a categorization tool of events in proton-proton collisions.
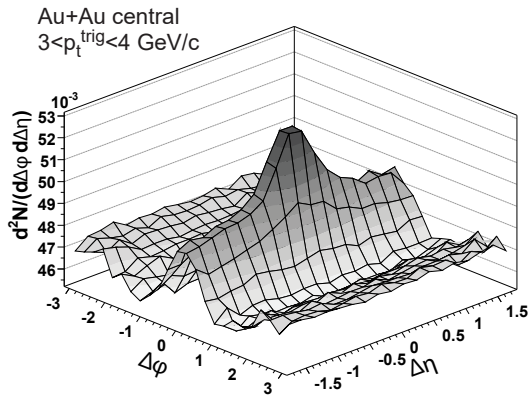

Figure 7: Long range correlation in $\Delta\eta$ appears as a ridge in the charged di-hadron distribution. Taken from the STAR collaboration at the Relativistic Heavy Ion Collider (RHIC). [14]

7 The LHC and ALICE

At the LHC (Fig. 8), protons and heavy ions are accelerated in stages. First the ions are extracted from the ion source with a strong electric field and then injected into the powerful linear accelerator (LINAC). In the LINAC varying electric fields in the drift tubes accelerate the ions until they reach the Proton Synchrotron Booster, which accelerate the particles further before injecting them into the Proton Synchrotron. The Proton Synchrotron (PS) is followed by the Super Proton Synchrotron (SPS), and they both stabilize the beam and further accelerate it with the help of superconducting magnets.

As the particles in the beam reach their maximal velocity they are ready to get injected into the LHC rings, where the collisions take place. The maximal collision energy at the LHC is $\sqrt{s} = 13$ TeV for proton-proton collisions and $\sqrt{s} = 5.02$ TeV, per nucleon pair, for heavy ion collisions. There are four large experiments situated around the LHC, at collision points of the beams: *LHCb*, *CMS*, *ATLAS* and *ALICE*.
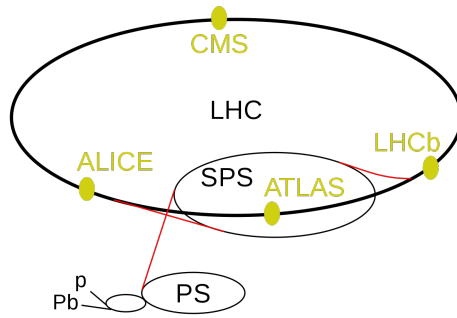
Figure 8: The LHC with the four experiments (*LHCb*, *CMS*, *ATLAS* and *ALICE*) around the ring. The synchrotrons (PS and SPS) and injection points are also visible. [15]

ALICE stands for *A Large Ion Collider Experiment* and it is a heavy-ion detector at the LHC, seen in Fig. 9. It focuses mainly on studying the strong interaction and the formation of QGP. The ALICE experiment consists of 18 different subdetectors, with different purposes. The detectors can be divided into the categories: *central barrel detectors*, *forward detectors* and the *muon spectrometer*.

In this thesis, only central barrel detectors were used to collect data. More specifically, the Inner Tracking System (ITS) and the Time Projection Chamber (TPC) were used to reconstruct the tracks analyzed here. Both of them only measure signals left by charged particles.[16]
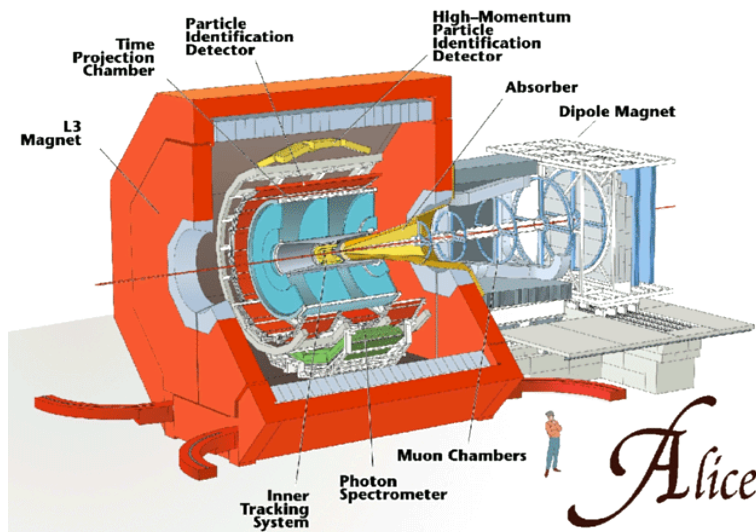

Figure 9: The ALICE detector and some of its subdetectors, including the Inner Tracking System and Time Projection Chamber. [17]

7.1 The Inner Tracking System (ITS)

The ITS is the detector nearest the beam line, at a radial distance of 3.9 cm $< r <$ 43 cm away from the beam. It consists of three types of layers, the Silicon Pixel Detector (SPD), the Silicon Drift Detector (SDD) and the Silicon Strip Detector (SSD). There are two layers of each type. The SPD layers are closest to the beam, at 3.9 cm and at 7.6 cm away from the beam. The SDDs are the intermediate layers of the ITS at 15 cm and 24 cm away from the beam. The SSDs, which are the outermost layers of the ITC, are at 38 cm and 43 cm away from the beam. All layers of the ITS detect signals from passing charged particles and are used along with the TPC to reconstruct the tracks. [18]

7.2 The Time Projection Chamber (TPC)

The TPC is the most important tracking detector in the central barrel. It finds tracks, identifies charged particles and measures their momenta as well. The TPC is a gas filled chamber with a volume of 88 m^3, the gas mixture is 90% Ne and 10% CO_2. At the center of the chamber, an electrode divides the the chamber into two symmetrical drift volumes. Charged particles passing through the gas will ionize it, leaving a trail of electrons that are drawn towards the cathode by the applied electric field. The electrons hit Multi-Wire Proportional Chambers and their arrival times are detected. The TPC identifies particles by using $< \frac{dE}{dx} >$ which is the average energy lost by a charged particle when traveling a distance dx. To measure the momentum, the TPC uses magnetic fields to curve the trajectory of the tracks in the azimuthal plane, which makes it possible to calculate the momenta of the charged particles.

8 Coordinates

In this section, the coordinate systems used in the analysis of high energy particle collisions are defined, as well as some observables which are useful in such relativistic events.

8.1 Angles and transverse momentum

Figure 10 is a sketch of the side and front view of the detector. In the side view we see a track, with momentum p and angle θ relative to the y-axis, leaving the tracking chamber. The beamline is defined to be the z-axis and the transverse plane (front view Fig. 10) is the x-y-plane. In the transverse plane, perpendicular to the beam axis, the angle between the transverse momentum vector and the y-axis is φ. The transverse momentum p_T is the part of the total momentum p moving in the transverse direction and is given by:

$$p_T = \sqrt{p_x^2 + p_y^2} \tag{2}$$

The transverse momentum can give information about what kind of event took place. Hard scattering yields higher transverse momentum transfer, whereas, soft scattering yields lower transverse momentum transfer. It is therefore a useful observable when looking for jets and categorizing events.
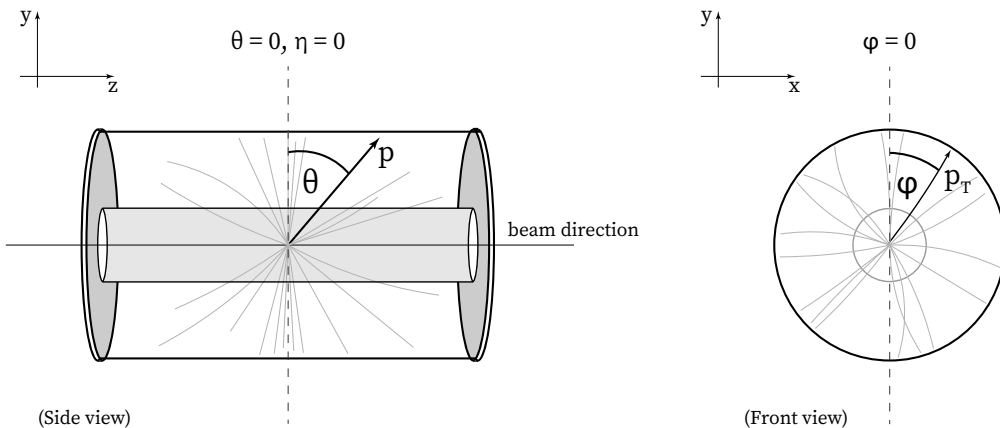

Figure 10: Left: Side view of the detector. A detected track and its trajectory through the detector in the y-z-plane. Right: The front view of the detector, the azimuthal plane. The same track traversing the x-y-plane of the detector.

8.2   Rapidity and pseudorapidity

Instead of polar angle θ , the rapidity y is convenient to use in relativistic events [5]. It is defined as:

$$y = \frac{1}{2} \ln \left(\frac{E + p_z}{E - p_z} \right) \tag{3}$$

However, at high enough energies when masses can be ignored, the *pseudorapidity* η can be used to approximate the rapidity.

$$y \approx \eta = -\ln \left(\tan \frac{\theta}{2} \right) \tag{4}$$

The pseudorapidity has a value of $\eta = 0$ for tracks traveling perpendicular to the beam axis, and $\eta = \infty$ for tracks traveling parallel to the beam axis. Particle production tends to be uniform in pseudorapidity for high energy scattering events. As seen in Fig. 10, the detector does not cover the entire pseudorapidity range since the detector is not surrounding the entire beam. Therefore, tracks can escape detection if the pseudorapidity is too high. In this thesis, an acceptance of $|\eta| < 0.8$ is used.

9 R_T

The azimuthal plane (x-y-plane) of the collision event is divided into three regions, as seen in Fig. 11. These regions are defined by the leading track, which is the detected track with highest transverse momentum in the event. The *toward* region is populated by tracks close to the leading track in the azimuthal plane, this region is assumed to contain the particles of the leading jet in the event. The *away* region is the opposite of the toward region, where the sub-leading jet is assumed to be. The *transverse* region is the region perpendicular to the jets, where there is high sensitivity to the UE. [9]
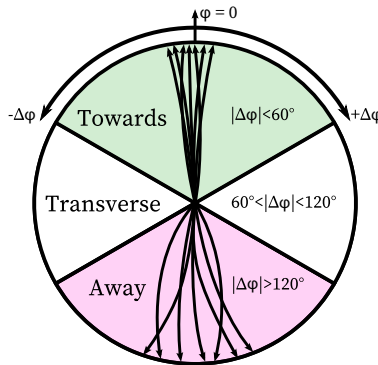

Figure 11: The three azimuthal regions as defined by the leading track. Each region covers an angle of $\frac{2\pi}{3}$, making the total sum of all three regions 2π. [10]

The relative transverse activity R_T is an observable that can be used to classify events in proton-proton collisions. R_T is sensitive to the UE, as it measures the transverse activity. R_T is defined as:

$$R_T = \frac{N_{ch}^{trans}}{< N_{ch}^{trans} >} \tag{5}$$

where N_{ch}^{trans} denotes the number of charged particles in the transverse region and $< N_{ch}^{trans} >$ is the average over all events, which makes it self-normalized. In this thesis, leading tracks (that define the regions) have a momentum range of $5 < p_T^{lead} < 40$ GeV/c and N_{ch}^{trans} is calculated from all tracks with lower transverse momentum than the leading track in the transverse region.

10   Two particle angular correlation

In this thesis, two particle angular correlation functions in $\Delta\eta$ and $\Delta\varphi$ will be investigated, for different values of R_T. The $\Delta\eta$ and $\Delta\varphi$ are defined as the differences in pseudorapidity, η, and azimuthal angle, φ, between the trigger and associated particles:

$$\Delta\eta = \eta_t - \eta_a \tag{6}$$

$$\Delta\varphi = \varphi_t - \varphi_a \tag{7}$$

The subscript t denotes the trigger track and a denotes the associated tracks. Correlation functions will be constructed in three configurations, where the selection of trigger and associated-tracks is varied. Trigger tracks are not equivalent to leading tracks. However, leading tracks can be chosen to be the trigger tracks, as with the first configuration.

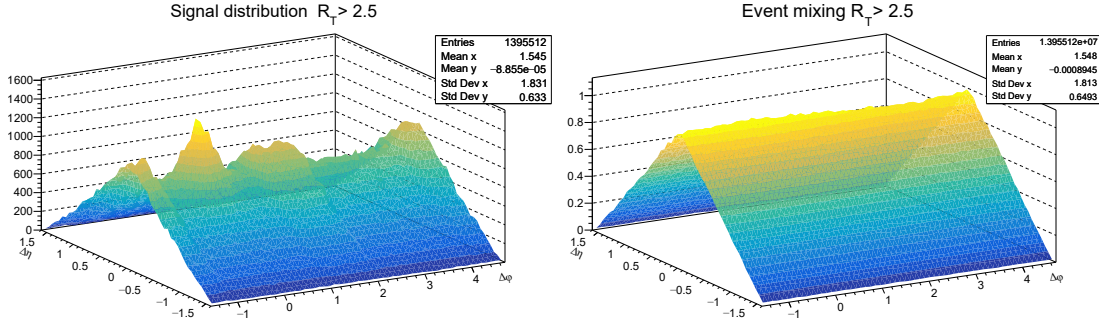## 10.1   Signal distribution and event mixing

Figure 12: Left: An example of a signal distribution from one of the configurations in this analysis. Right: The event mixing belonging to the signal event distribution on the left. The per-trigger correlation is given by dividing the signal distribution by the mixed event distribution.

The per-trigger-particle signal distribution $S(\Delta\eta, \Delta\varphi)$ is constructed by selecting a trigger, or a transverse momentum range for the triggers, and a transverse momentum range for associated tracks. All possible pairs between trigger and associated tracks are then formed and the following distribution is constructed, where N^{pair} is the number of same event pairs and $N^{trigger}$ is the number of triggers used to create the distribution:

$$S(\Delta\eta, \Delta\varphi) = \frac{1}{N^{trigger}} \frac{d^2 N^{pair}}{d\Delta\eta d\Delta\varphi} \tag{8}$$

The mixed event distribution $B(\Delta\eta, \Delta\varphi)$ uses the same triggers, although when mixing, the associated tracks are taken from other uncorrelated events. This is done to measure the acceptance of the detector and to have an uncorrelated reference to normalize with. The mixed event distribution is given by:

$$B(\Delta\eta, \Delta\varphi) = \frac{d^2 N^{mixed}}{d\Delta\eta d\Delta\varphi} \tag{9}$$

where N^{mixed} is the number of mixed event pairs. In this analysis, each event will be mixed with ten other uncorrelated events and the final mixed distributions will be normalized to unity at $(\Delta\eta = 0, \Delta\varphi = 0)$. Examples of signal and background distributions can be seen in Fig. 12.

The per-trigger yield correlation function is used to compute the average number of associated tracks that are correlated with every trigger track, and is defined as:

$$Y(\Delta\eta, \Delta\varphi) = \frac{S(\Delta\eta, \Delta\varphi)}{B(\Delta\eta, \Delta\varphi)} \tag{10}$$

11 Analysis

The analyzed data was collected in proton-proton collisions by the ALICE detector in the LHC in 2016, at a center-of-mass energy of $\sqrt{s} = 13$ TeV. A total of approximately 120 million events were available, although not all events were used due to some events failing to meet some criteria. A total of four criteria were used for events.

- Events must have at least one track.

- Pileup-events are discarded.

- Each event must have a vertex in the range -10 cm $< v_z < 10$ cm.

- Each event must have a leading track in the range $5.0 < p_T < 40.0$ GeV/c.

Pileup events are events which happen in quick succession and leave overlapping signals in the detector. This is mainly due to the large rate of events and the shortcomings of the detector to separate them and find a vertex for each event. After checking these criteria, approximately 1.7 million events remained. Table 1 below details how many events were excluded and for what reason.

Table 1: The number of events excluded due to the set criteria. The large bulk of events excluded were due to the absence of a leading track in those events.

Events with no tracks	Pileup-events	Events without a vertex	Events with vertex outside range	Events with no leading track
2,240,420	0	2,386,294	2,932,852	110,436,071

The correlation functions are not yet corrected for tracking efficiency, therefore the particle yields are underestimated by approximately 10%. However it does not depend on R_T, and will be neglected in the analysis.

11.1 Trigger and associated track selection

As mentioned, the correlation function will be constructed three times with different trigger and associated track configurations. The first time (*Configuration 1*), the leading track of the event will be the one and only trigger track for the event. The second time (*Configuration 2*), multiple triggers per event will be allowed and are selected from a chosen transverse momentum range. The third time (*Configuration 3*), correlations within the three azimuthal regions will be investigated, where the triggers and associated tracks must be in the same region. The chosen transverse momentum ranges for the trigger and associated tracks, for all three configurations, can be seen in Table 2. Because of the detector acceptance mentioned in section 7.2, only tracks with $|\eta| < 0.8$ are accepted.

Table 2: Trigger and associated track selection, for all three configurations.

Configuration	Transverse momentum range: trigger tracks (GeV/c)	Transverse momentum range: associated tracks (GeV/c)
Configuration 1	$5.0 < p_T < 40.0$	$0.5 < p_T < 5.0$
Configuration 2	$3.0 < p_T < 5.0$	$0.5 < p_T < 3.0$
Configuration 3	$3.0 < p_T < 5.0$	$0.5 < p_T < 3.0$

When mixing events, in all configurations, the associated tracks from the uncorrelated events had to be from events within the same R_T range. Furthermore, (in *Configuration 1*) the momentum bins were also taken into account when mixing, such that no track outside the momentum bin would be mixed in.

When performing the event mixing in *Configuration 3*, trigger tracks were mixed with associated tracks that were in the same region as the trigger track, as defined by the leading track of the trigger track event instead of the leading track of its own event. As the mixing is done to measure the acceptance of the detector with uncorrelated events, this was deemed to be the optimal way to mix the events for *Configuration 3*.

12 Results

In the following sections, the results of the two-particle angular correlations are presented. The results are divided into three parts: we firstly look at the results from the correlation functions with respect to the leading tracks, secondly with trigger tracks from a selected range which does not include the leading track, and finally the correlations in the three different regions.

Only the $\Delta\eta$ and $\Delta\varphi$-projections of the two-dimensional correlation functions will be shown in the result section. The 2D-plots of the correlation functions can be seen in the Appendix. The results of the R_T calculation for all events can be seen in Table 3 below. $<N_{ch}^{trans}>$ (Eq. 5) was calculated to be $<N_{ch}^{trans}>\approx 6.14$.

Table 3: Total number of events within a given R_T range.

$R_T < 0.3$	$0.3 < R_T < 0.5$	$0.5 < R_T < 1.0$	$1.0 < R_T < 1.5$	$1.5 < R_T < 2.0$	$2.0 < R_T < 2.5$	$R_T > 2.5$
241,183	363,683	483,838	315,379	177,469	93,073	86,571

The projections in $\Delta\varphi$ have a range of $(-\frac{\pi}{2} < \Delta\varphi < 3\frac{\pi}{2})$, covering a total of 2π. They are shifted from the common range $(0 < \Delta\varphi < 2\pi)$ to make analysis easier, since we expect a large peak at $\Delta\varphi = 0$. The $\Delta\varphi$-range is divided into sub-ranges: the *near-side* is defined as the range $(-\frac{\pi}{3} < \Delta\varphi < \frac{\pi}{3})$, the *away-side* is defined as the range $(2\frac{\pi}{3} < \Delta\varphi < 4\frac{\pi}{3})$, and the *transverse-regions* are everything in between the near and away sides, and are defined as the ranges $(\frac{\pi}{3} < |\Delta\varphi| < 2\frac{\pi}{3})$. Notice the absolute value in the range of the transverse-regions, which includes the positive and negative ranges.

The $\Delta\eta$-projections have a range of $(-1.6 < \Delta\eta < 1.6)$. Although, the far edges of this range have a high statistical uncertainty, sometimes referred to as *wings* due to the shape they take. Therefore, the range of $\Delta\eta$ is restricted to $(-1 < \Delta\eta < 1)$ when taking the projections in $\Delta\varphi$.

12.1 Configuration 1

In this section we present the $\Delta\eta$ and $\Delta\varphi$-projections, including all R_T and p_T bins, for the correlation function with respect to the leading tracks. The transverse momentum bins are defined in Table 4 below.

The $\Delta\varphi$-projections of the three different p_T bins (Fig. 13) as well as the the $\Delta\eta$-projections can be seen below. $\Delta\eta$-projections were divided up into near-side (Fig. 14) and away-side (Fig. 15) in order to try to see how the peak at $\Delta\eta = 0$, corresponding to the jets, changes with R_T.

Table 4: Trigger selection and momentum bins for associated tracks, in *Configuration 1*.

Transverse momentum range: trigger tracks (GeV/c)	Transverse momentum range: associated tracks, low p_T bin (GeV/c)	Transverse momentum range: associated tracks, mid p_T bin (GeV/c)	Transverse momentum range: associated tracks, high p_T bin (GeV/c)
5.0 < pT < 40.0	0.5 < pT < 1.0	1.0 < pT < 3.0	3.0 < pT < 5.0

The selected events with $R_T < 1$ have a larger peak in the near-side of the $\Delta\varphi$-projections, indicating a more significant jet fragmentation for events with lower R_T and higher p_T-transfer ranges. On the away-side, a shorter and broader peak can be seen for low R_T, consistent with back-to-back jet signals. With higher R_T, the away-side peak flattens out and a significant rise in the transverse region can be observed.

$\Delta\varphi$-projections in the mid-R_T bins, around $R_T = 1$, are close to continuous, which is expected since the average R_T is 1. The discontinuity observed in the bins higher or lower than the average indicate autocorrelation which is a sign that events are being selected with a bias, as expected. In the transverse region the distribution is not entirely flat when approaching the edges of the region. Some of this may be an effect of the toward and away-side bleeding in to the transverse region.

There are some differences between high and low transverse momentum bins. The most obvious is the typical near-side peak which is visible in all momentum bins, but as would be expected, this peak is most dominating in the highest bin ($3.0 < p_T^{assoc} < 5.0$ GeV/c) and decreases in the lower bins.

Another difference in the p_T bins is the transverse region, where there is higher correlation in the lower p_T bins than the higher bins. Higher transverse momentum transfer events (hard scatter events) should show less correlation in the transverse region, however, there is still a visible rise in the transverse region for the three highest R_T bins ($R_T > 1.5$). The away-side peak gets less flattened in the highest p_T bin than the lower ones. This effect is most noticeable in the higher R_T bins.

The $\Delta\eta$-projections do not seem to indicate any significant changes to the peak at $\Delta\eta = 0$ in the near-side for different R_T. It is, however, visible that the peaks for lower R_T are lower and sharper than the peaks for higher R_T. The distribution in the away-side is mostly uniform for all bins.
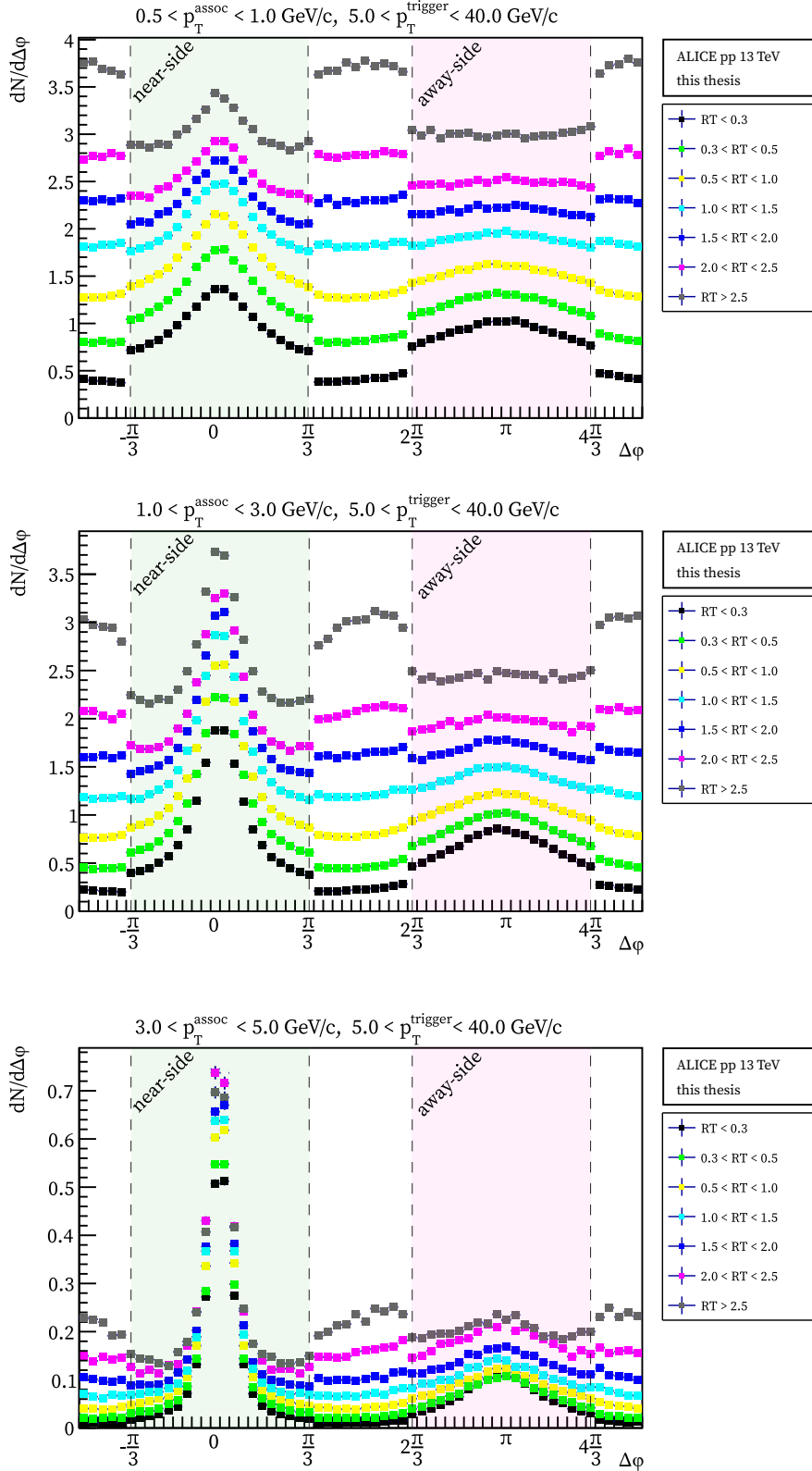
Figure 13: $\Delta\varphi$-projections of the correlation function, with *Configuration 1*. Top: Low p_T bin $(0.5 < p_T^{assoc} < 1.0$ GeV). Middle: Mid p_T bin $(1.0 < p_T^{assoc} < 3.0$ GeV). Bottom: High p_T bin $(3.0 < p_T^{assoc} < 5.0$ GeV). The near and away-sides are indicated with shaded regions.
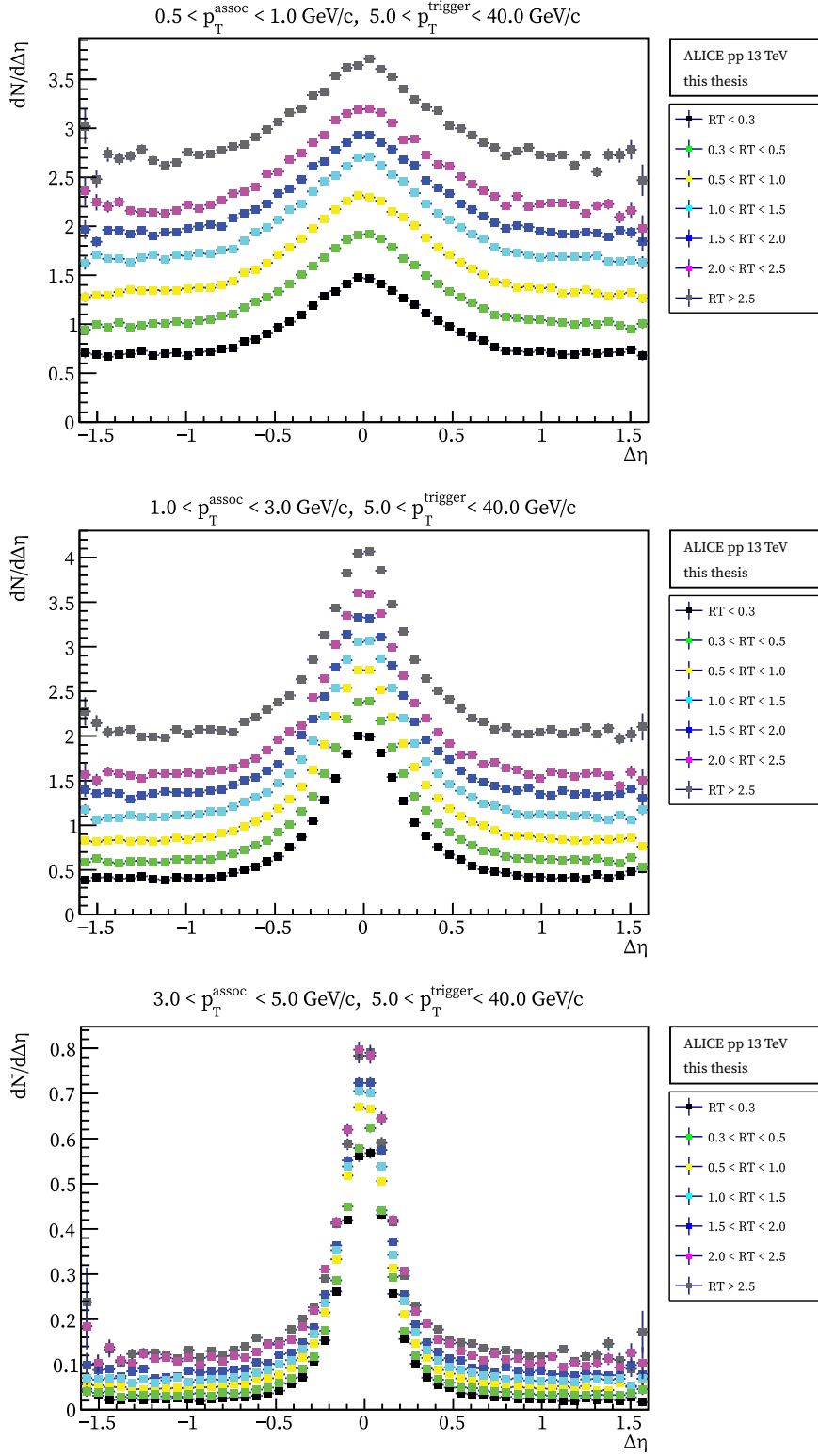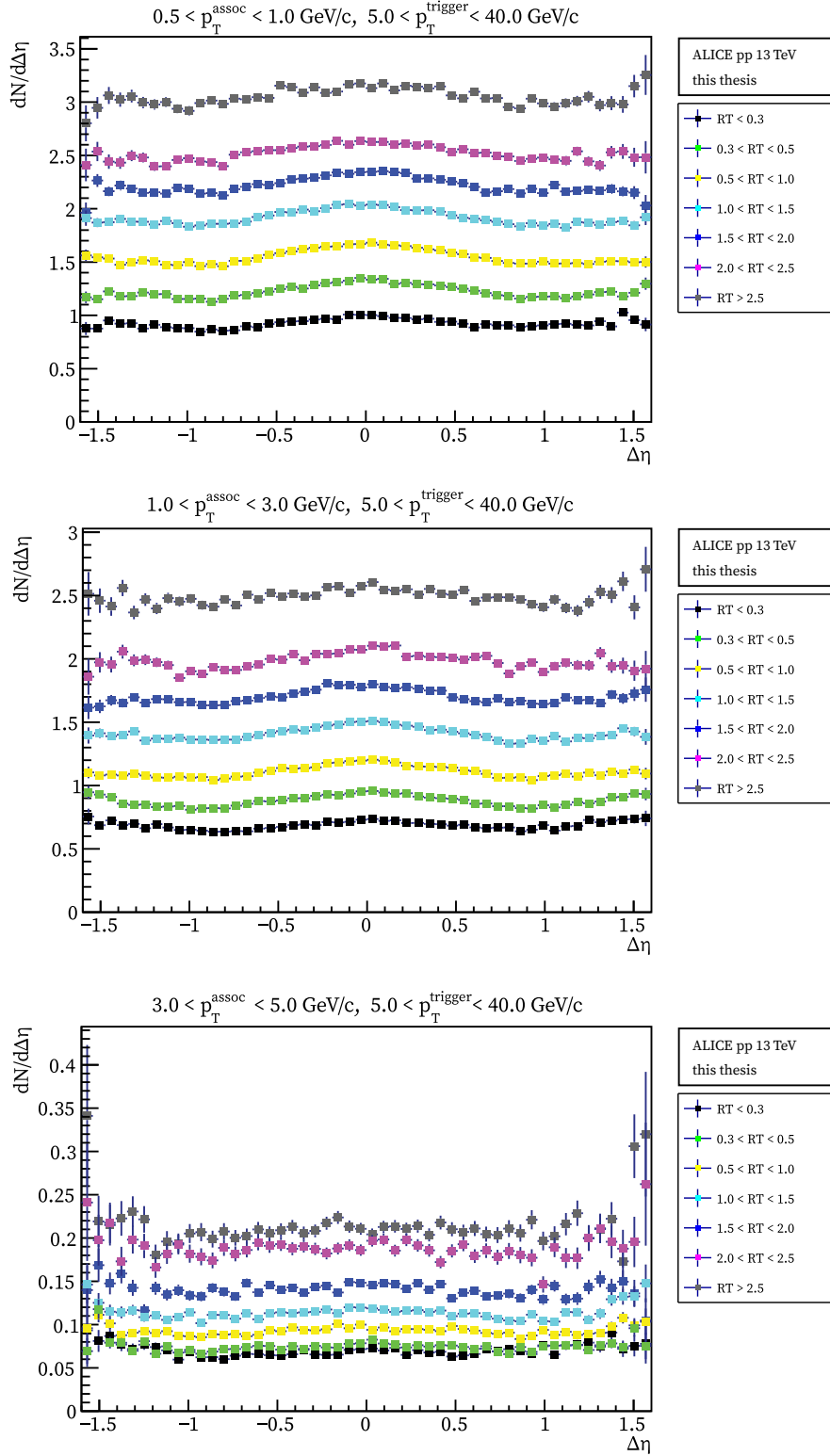
Figure 14: $\Delta\eta$-projections (restricted to the near-side of $\Delta\varphi$) of the correlation function, with *Configuration 1*. Top: Low p_T bin ($0.5 < p_T^{assoc} < 1.0$ GeV/c). Middle: Mid p_T bin ($1.0 < p_T^{assoc} < 3.0$ GeV/c). Bottom: High p_T bin ($3.0 < p_T^{assoc} < 5.0$ GeV/c).

Figure 15: $\Delta\eta$-projections (restricted to the away-side of $\Delta\varphi$) of the correlation function, with *Configuration 1.* Top: Low p_T bin ($0.5 < p_T^{assoc} < 1.0$ GeV/c). Middle: Mid p_T bin ($1.0 < p_T^{assoc} < 3.0$ GeV/c). Bottom: High p_T bin ($3.0 < p_T^{assoc} < 5.0$ GeV/c).

12.2 Configuration 2

The $\Delta\varphi$ (Fig. 16) and $\Delta\eta$-projections (Fig. 17) of the correlation function with the following track selection:

$$3.0 < p_T^{trigger} < 5.0 \text{ GeV/c}, \qquad 0.5 < p_T^{assoc} < 3.0 \text{ GeV/c}$$

are presented in this section. Here, the triggers belong to a separate and lower transverse momentum range than the leading tracks. This minimizes the risk of introducing bias.

A feature that sticks out in the $\Delta\varphi$-projections is the flattening of the away-side peak for higher R_T. The near-side peak decreases as well, although the effect is not as drastic. The transverse region shows less correlation for lower R_T than higher R_T, however, the rise is not as substantial as in *Configuration 1*. There does not seem to be any discontinuities in the $\Delta\phi$-projections, as was the case in the first configuration.

Similar to the first configuration, the $\Delta\eta$-projections do not seem to indicate any significant changes to the near-side or away-side for different R_T in this configuration either.
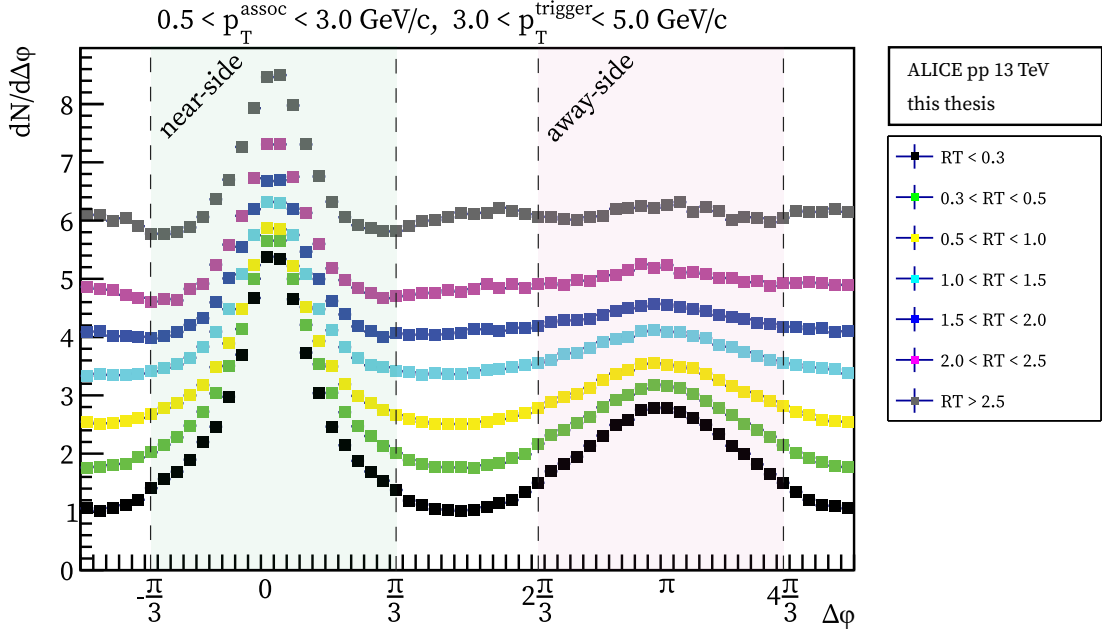
Figure 16: $\Delta\varphi$-projections of the correlation function, with *Configuration 2*. The near and away-sides are indicated with shaded regions.
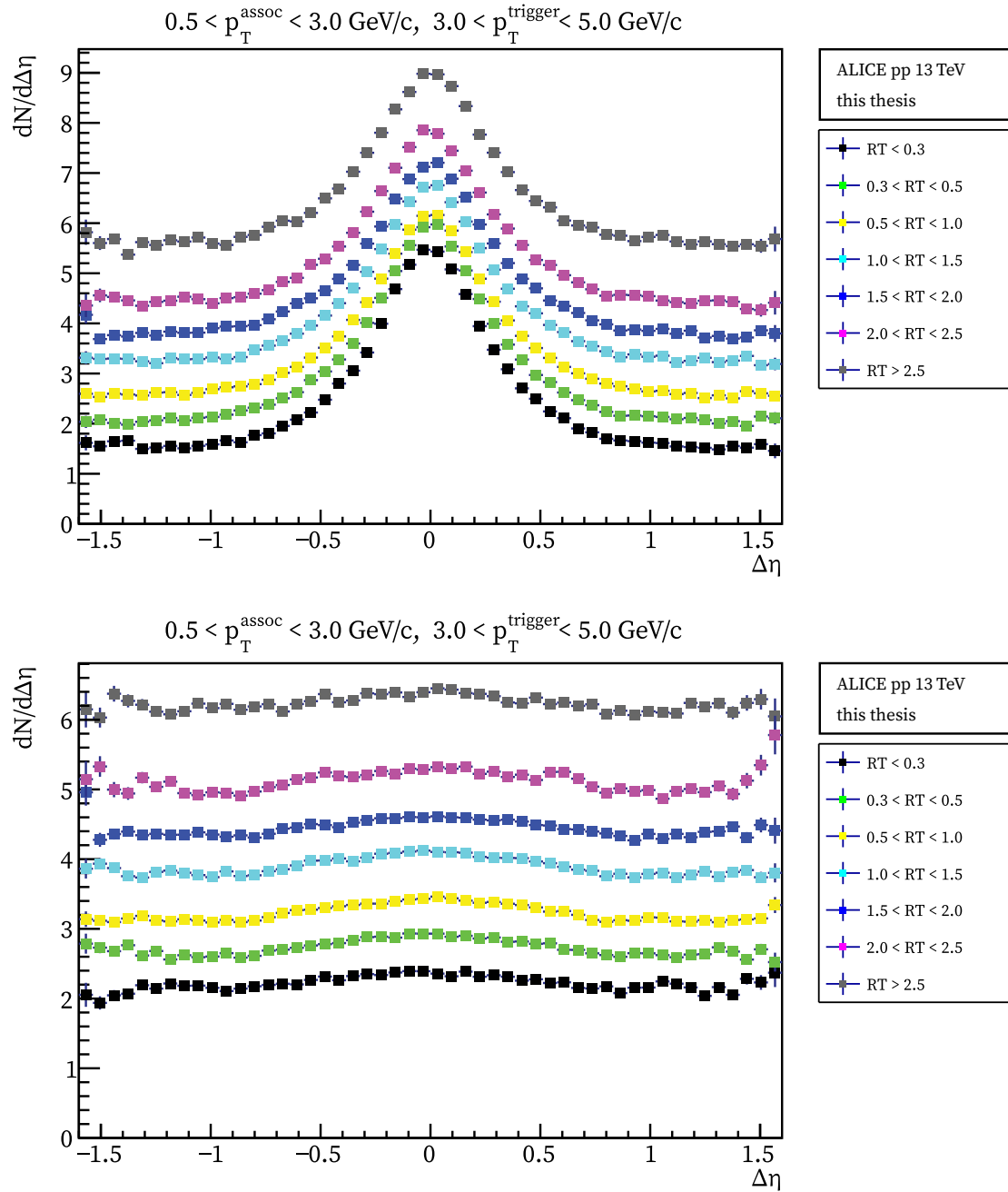
Figure 17: $\Delta\eta$-projections of the correlation function, with *Configuration 2*. Top: Restricted to the near-side of $\Delta\varphi$. Bottom: Restricted to the away-side of $\Delta\varphi$.

12.3 Configuration 3

Here, the $\Delta\varphi$ (Fig. 18) and $\Delta\eta$-projections (Fig. 19) of the correlation functions in the azimuthal regions are presented. The transverse momentum ranges for the track selections were the following:

$$3.0 < p_T^{trigger} < 5.0 \text{ GeV/c}, \qquad 0.5 < p_T^{assoc} < 3.0 \text{ GeV/c}$$

This section is divided into three parts, corresponding to the three azimuthal regions: toward, transverse and away. The same momentum ranges were used in all regions.

12.3.1 Transverse region

Projections in $\Delta\varphi$, of the transverse region, show a peak at $\Delta\varphi = 0$ which grows with increasing R_T. There is no corresponding peak at $\Delta\varphi = \pi$, where one might expect a peak if the peak at $\Delta\varphi = 0$ are due to mini-jets. Conservation of momentum should then yield a peak in the opposite direction of the mini-jets. This could be due the selection of transverse momentum ranges or the chosen R_T cuts. An interesting result is that we see some correlation even for the low R_T bin ($0.3 < R_T < 0.5$), where the UE is expected to be small.

In order to make a correlation, there has to be at least two tracks in the transverse region ($N_{ch}^{trans} \geq 2$). The average number of transverse tracks ($< N_{ch}^{trans} >$) was calculated to be 6.14. Using the definition of R_T (Eq. 5) with the lowest R_T bin ($R_T < 0.3$), we see that we will not find an event with $N_{ch}^{trans} \geq 2$:

$$R_T < 0.3 \implies \frac{N_{ch}^{trans}}{< N_{ch}^{trans} >} < 0.3 \implies N_{ch}^{trans} < 0.3 \cdot 6.14 \implies N_{ch}^{trans} < 1.8 \qquad (11)$$

Thus, there is no data in the plot for that bin in the transverse region.

The $\Delta\eta$-projections show some differences for different R_T. Lower R_T bins have a flatter distribution, while the higher R_T bins grow a peak at $\Delta\eta = 0$. The $\Delta\eta$-projections are not as smooth and uniform as in the two previous configurations, this is most likely due to low statistics.
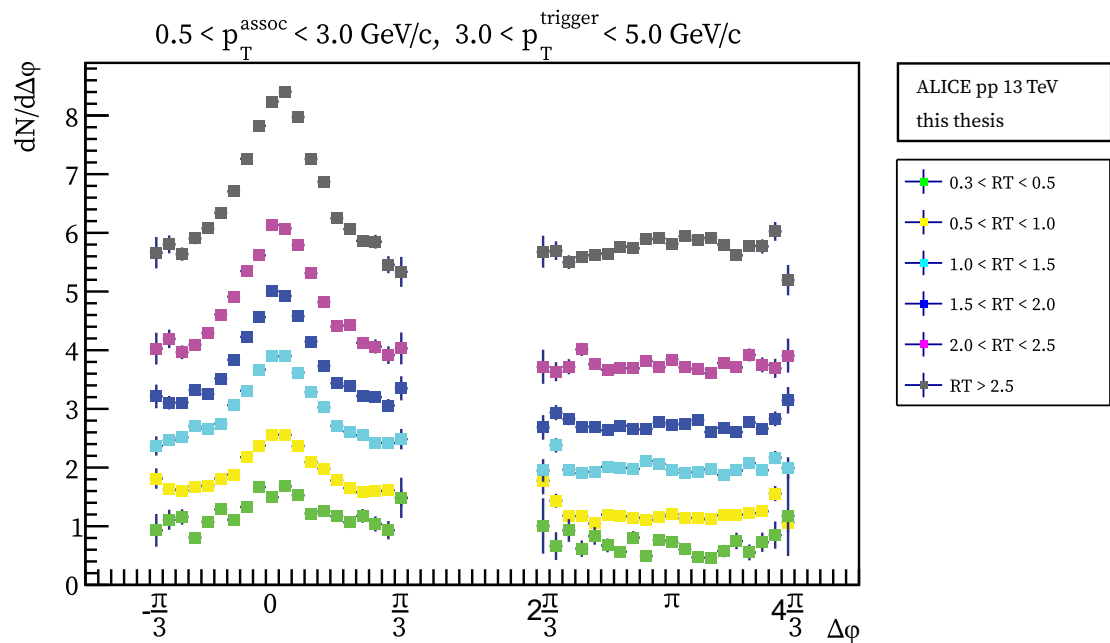
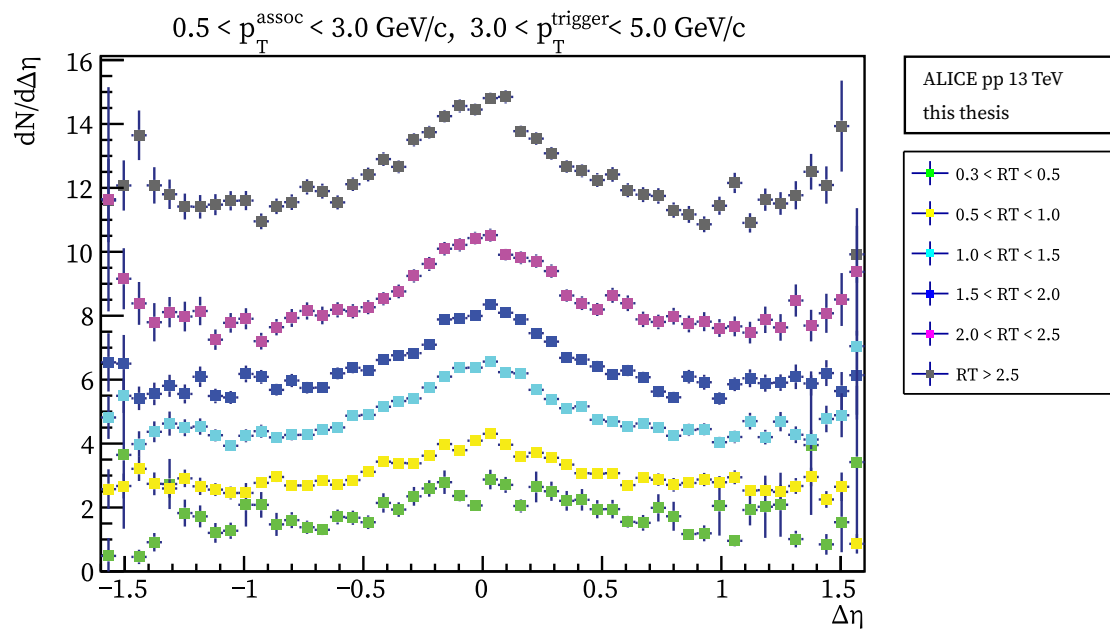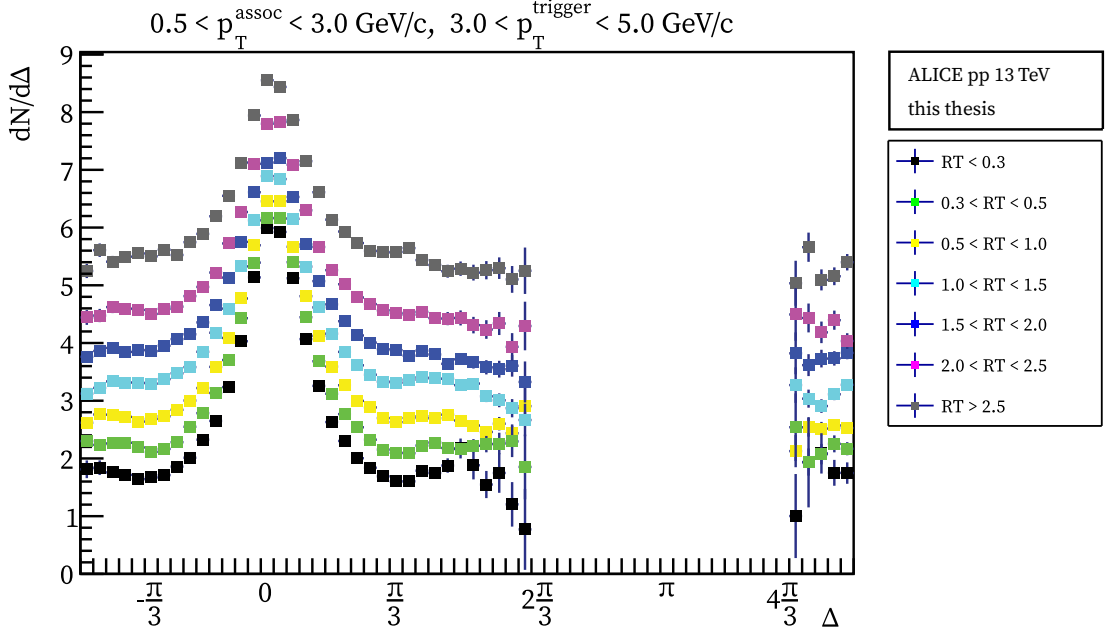Figure 18: $\Delta\varphi$-projections of the correlation function with *Configuration 3*. Transverse region.

Figure 19: $\Delta\eta$-projections of the correlation function with *Configuration 3*. Transverse region.

12.3.2 Toward region

In the toward region, the $\Delta\varphi$-projections (Fig. 20) show a peak at $\Delta\varphi = 0$ which decreases with increasing R_T. This is consistent with larger UE for higher values of R_T. The $\Delta\eta$-projections show a peak at $\Delta\eta = 0$ for all R_T bins. There does not seem to be a significant difference for different R_T.
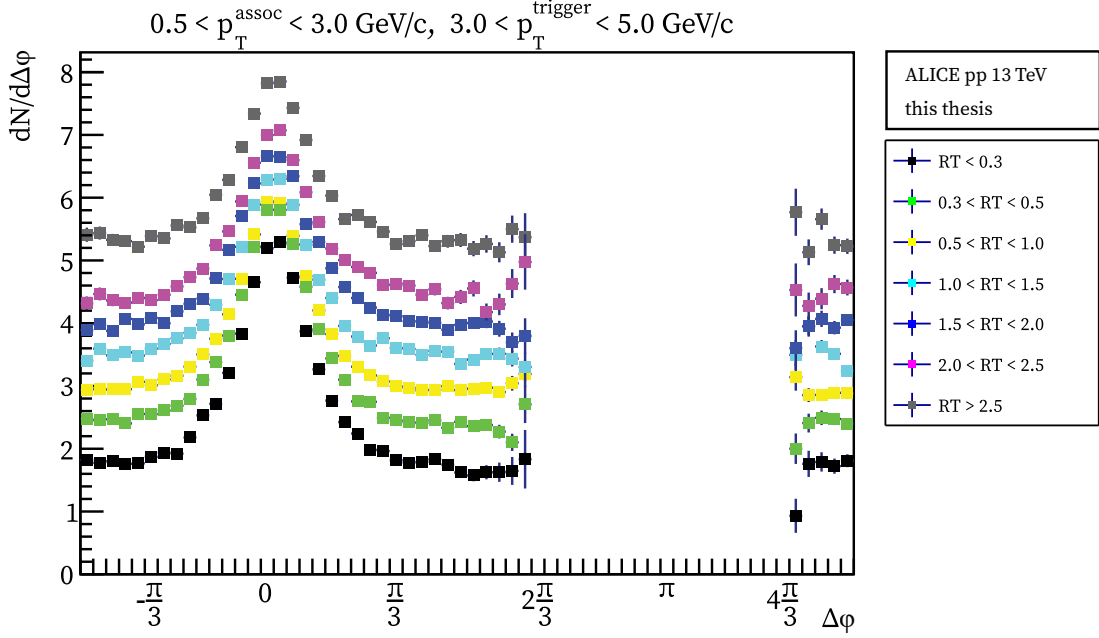

Figure 20: $\Delta\varphi$-projections of the correlation function with *Configuration 3*. Toward region.
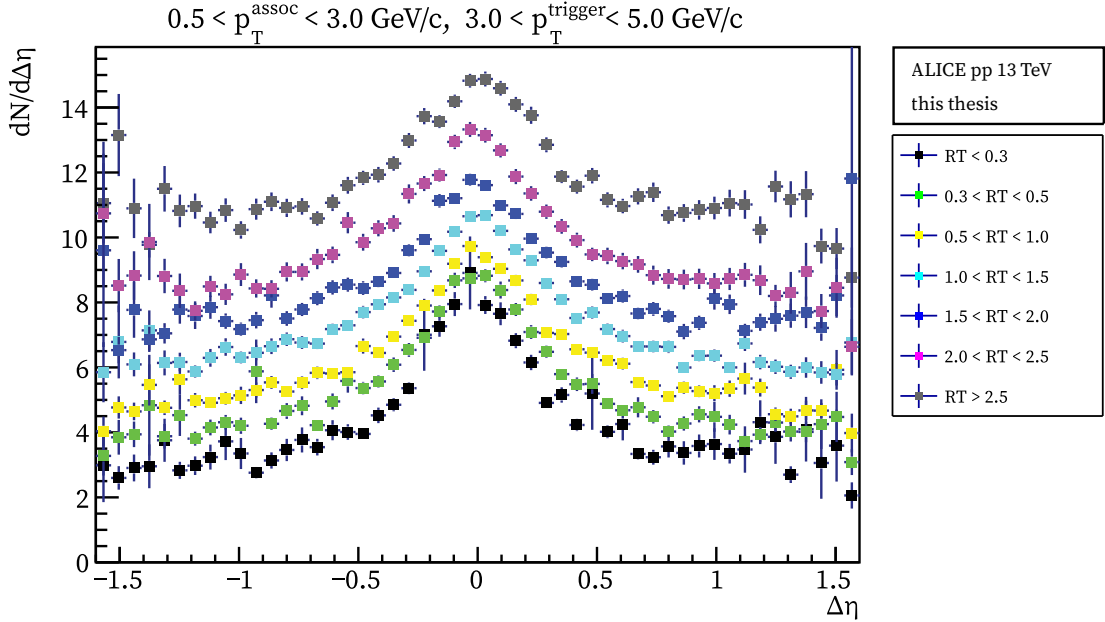
Figure 21: $\Delta\eta$-projections of the correlation function with *Configuration 3*. Toward region.

12.3.3   Away region

The away region displays similar features as the toward region, with similar peaks in both $\Delta\varphi$ and $\Delta\eta$-projections at $(\Delta\varphi = 0)$ and $(\Delta\eta = 0)$ respectively. The peaks, in both projections, decrease with increasing R_T.

Figure 22: $\Delta\varphi$-projections of the correlation function with *Configuration 3*. Away region.
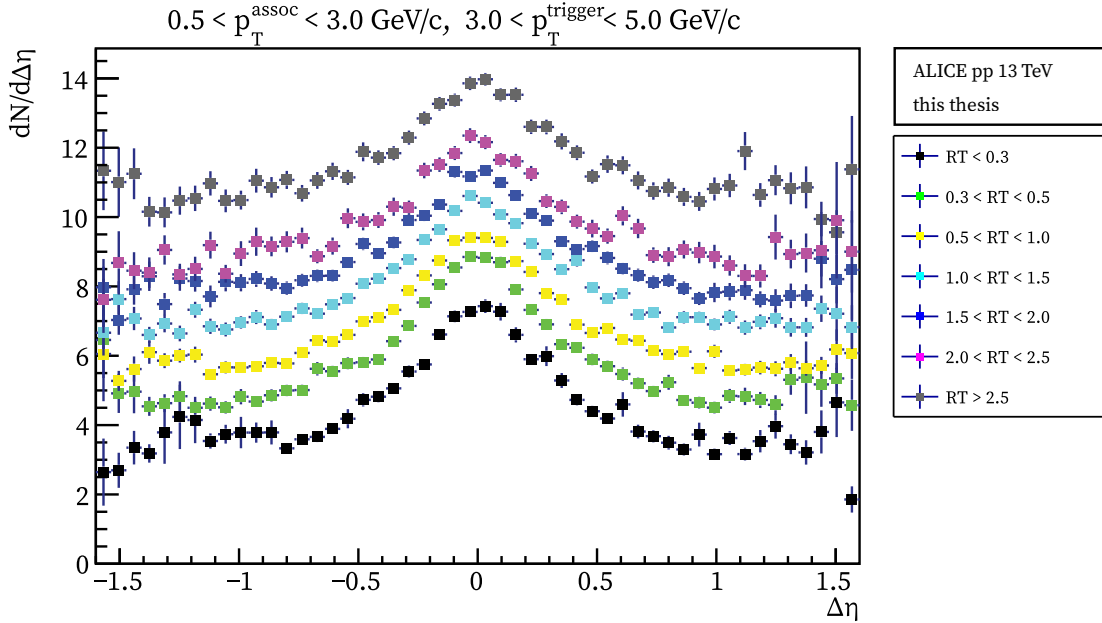

Figure 23: $\Delta\eta$-projections of the correlation function with *Configuration 3*. Away region.

13 Conclusion and outlook

In all three configurations, events with low R_T are dominated by back-to-back jet (or mini-jet) fragmentation structures, while events with higher R_T show a large activity in the transverse region and lower (sometimes disappearing) away-side peak. The significant near-side correlation found in the transverse region (*Configuration 3*) suggests that R_T might not be selecting event topologies with isotropic bulk particle production, which was not expected.

From *Configuration 1* we see that higher R_T yields a higher particle yield in the transverse region. The opposite is true for lower R_T, where the correlation in the transverse region decreases. This indicates that R_T selects event shapes with sensitivity to the UE, which was expected by this observable. For high transverse momentum bins we see less correlation in the transverse region, however, there is still a significant correlation for the highest R_T bin. Higher transverse momentum bins should be investigated to see at what momentum range this effect diminishes.

Further investigation should be done in order to understand why the away-side peak in the $\Delta\varphi$-projections (of *Configuration 1* and *Configuration 2*) vanishes with higher R_T. This should be done with additional R_T ranges in the low and high values to see what happens at the extremes. A suggestion would be to look into subranges above $R_T > 4.0$ and below $R_T < 0.3$. One should also redo *Configuration 2* with several transverse momentum ranges for the associated tracks, as only one bin range did not reveal enough for a conclusion to be made. The trigger track selection can be redefined to include higher transverse momentum ranges, to see if the away-side peak reappears for those ranges. This analysis investigated correlations as a function of transverse multiplicity (N_{ch}^{trans}). Using the total multiplicity, instead of just the transverse multiplicity, might help us understand what makes the away-side peak disappear.

Since the average number of transverse tracks ($< N_{ch}^{trans} >= 6.14$) is quite low in this analysis, other momentum ranges for the leading tracks could be implemented in order to get a higher $< N_{ch}^{trans} >$. This would be preferable when doing correlations in the transverse region, since it would increase the probability of having at least two tracks in the transverse region, which is required for two-particle correlations to be possible. It would also be interesting to see how the away-side peaks in the $\Delta\varphi$-projections (of *Configuration 1* and *Configuration 2*) would change, with a definition of R_T which has a higher average number of transverse tracks.

In the $\Delta\varphi$-projection of *Configuration 3*, for the transverse region, there was only a peak at $\Delta\varphi = 0$ and no clear corresponding peak at $\Delta\varphi = \pi$. This effect, is not understood in this analysis and should be further investigated. As mentioned, a redefinition of R_T could yield more data for the analysis in the transverse region. Furthermore, subdividing the transverse momentum range for the associated tracks could shine some light on why there is no peak at $\Delta\varphi = \pi$.

References

[1] Gines Martinez. "Advances in Quark Gluon Plasma". In: (2013). arXiv: 1304.1452 [nucl-ex].

[2] Dragos Velicanu. "Ridge correlation structure in high multiplicity pp collisions with CMS". In: (2011). arXiv: 1107.2196 [nucl-ex].

[3] Adrian Dumitru et al. "The ridge in proton-proton collisions at the LHC". In: (2010). arXiv: 1009.5295 [hep-ph].

[4] B.R. Martin and G. Shaw. *Particle Physics*. Manchester Physics Series. Wiley, 2008. ISBN: 9780470721537. URL: https://books.google.se/books?id=whIbrWJdEJQC.

[5] Giles Barr et al. *Particle physics in the LHC era*. Oxford master series in particle physics, astrophysics and cosmology. Oxford: Oxford University Press, 2016. DOI: 10.1093/acprof: oso/9780198748557.001.0001. URL: https://cds.cern.ch/record/2034442.

[6] MissMJ. *Wikimedia Commons*. Sept. 2019. URL: https://upload.wikimedia.org/wikipedia/commons/0/00/Standard_Model_of_Elementary_Particles.svg.

[7] J M Campbell, J W Huston, and W J Stirling. "Hard interactions of quarks and gluons: a primer for LHC physics". In: *Reports on Progress in Physics* 70.1 (Dec. 2006), pp. 89–193. ISSN: 1361-6633. DOI: 10.1088/0034-4885/70/1/r02. URL: http://dx.doi.org/10.1088/0034-4885/70/1/R02.

[8] D. Wilson R. Field C. Group. *The Energy Dependence of Min-Bias and the Underlying Event at CDF*. 2012. URL: https://www-cdf.fnal.gov/physics/new/qcd/ue_escan/. Retrieved: 2020-05-10.

[9] T. Affolder et al. "Charged jet evolution and the underlying event in proton-antiproton collisions at 1.8 TeV". In: *Phys. Rev. D* 65 (9 Apr. 2002), p. 092002. DOI: 10.1103/PhysRevD.65.092002. URL: https://link.aps.org/doi/10.1103/PhysRevD.65.092002.

[10] Tim Martin, Peter Skands, and Sinead Farrington. *Probing Collective Effects in Hadronisation with the Extremes of the Underlying Event*. 2016. arXiv: 1603.05298 [hep-ph].

[11] Cerncourier. *Participants and spectators at the heavy ion fireball*. 2013. URL: https://cerncourier.com/a/participants-and-spectators-at-the-heavy-ion-fireball/. Retrieved: 2020-05-10.

[12] Wit Busza, Krishna Rajagopal, and Wilke van der Schee. "Heavy Ion Collisions: The Big Picture, and the Big Questions". In: (2018). arXiv: 1802.04801 [hep-ph].

[13] B. Alver and G. Roland. "Collision geometry fluctuations and triangular flow in heavy-ion collisions". In: (2010). arXiv: 1003.0194 [nucl-th].

[14] The STAR Collaboration and B. I. Abelev. "Long range rapidity correlations and jet production in high energy nuclear collisions". In: (2009). arXiv: 0909.0191 [nucl-ex].

[15] Arpad Horvath. *The LHC*. Apr. 2006. URL: https://sv.wikipedia.org/wiki/Large_Hadron_Collider#/media/Fil:LHC.svg. Retrieved: 2020-05-10.

[16] ALICE Collaboration. "Performance of the ALICE Experiment at the CERN LHC". In: (2014). arXiv: 1402.4476 [nucl-ex].

[17] Lund University Department of Physics. *ALICE*. Oct. 2013. URL: https://www.hep.lu.se/alice/. Retrieved: 2020-05-10.

[18] ALICE Collaboration. *More details on the ALICE ITS*. URL: http://alice.web.cern.ch/detectors/more-details-alice-its. Retrieved: 2020-05-10.
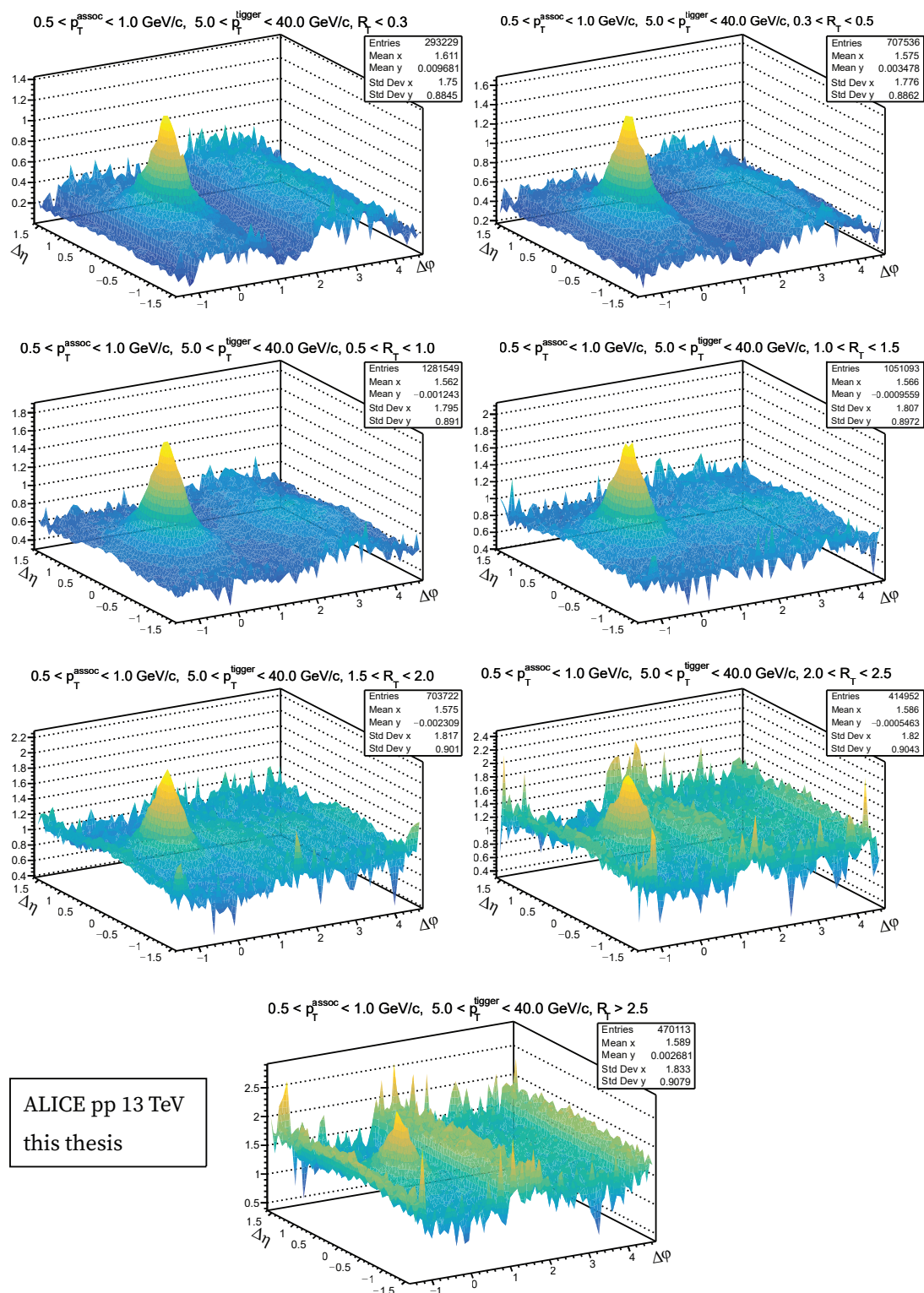
A   Appendix

Figure 24: *Configuration 1*: Per-trigger correlation functions in $(\Delta\eta, \Delta\varphi)$ for different R_T, for the lowest transverse momentum bin $(0.5 < p_T^{assoc} < 1.0$ GeV/c).
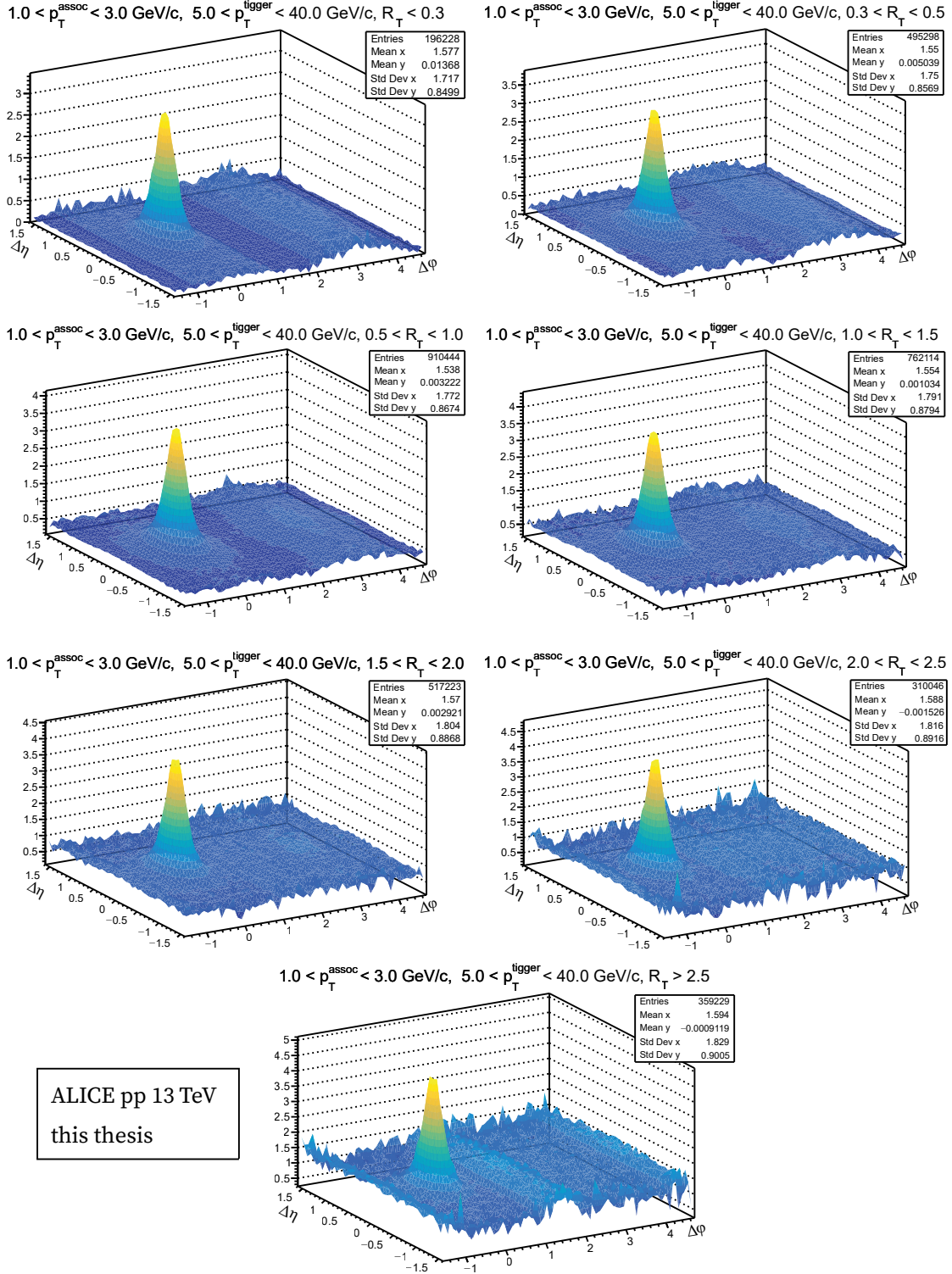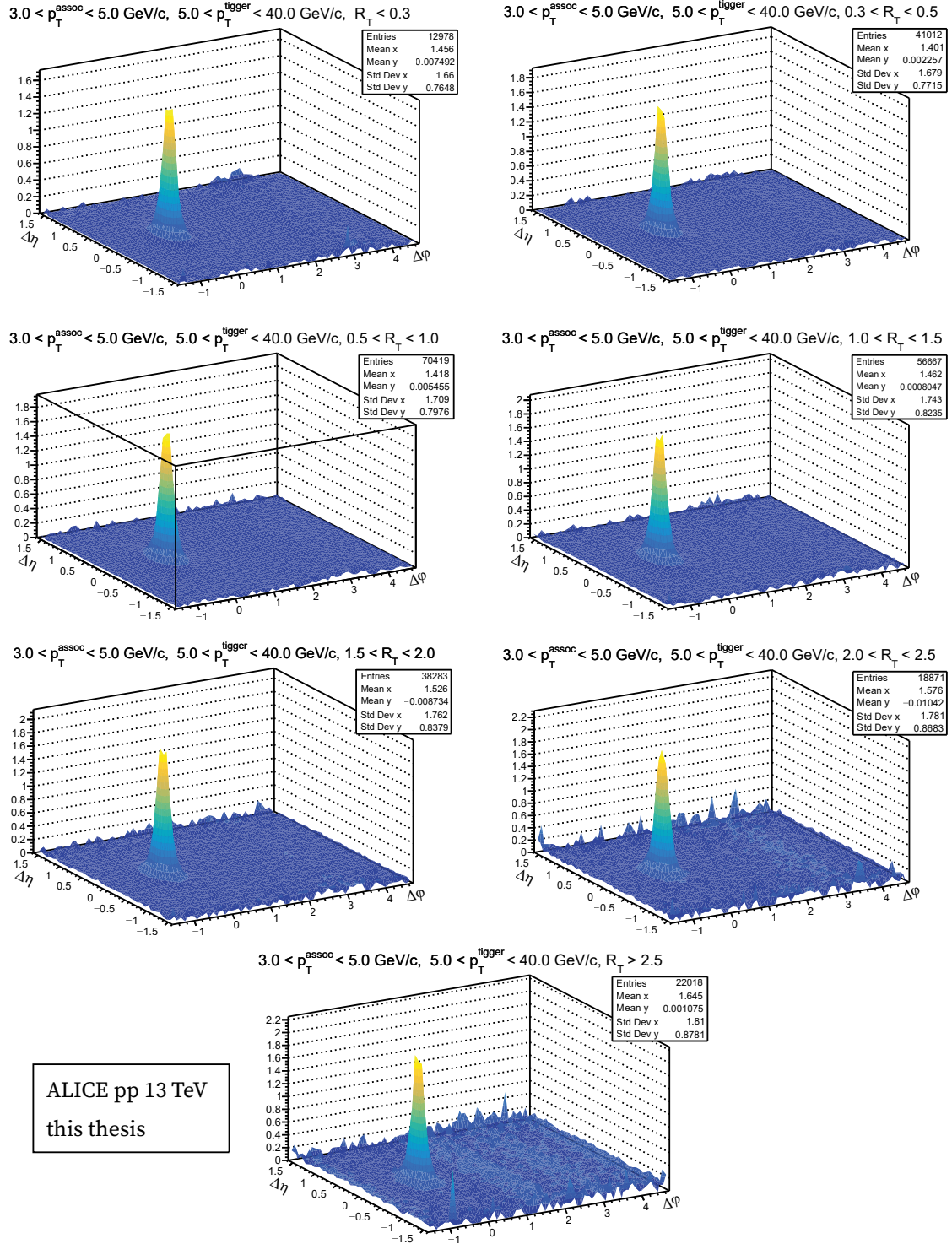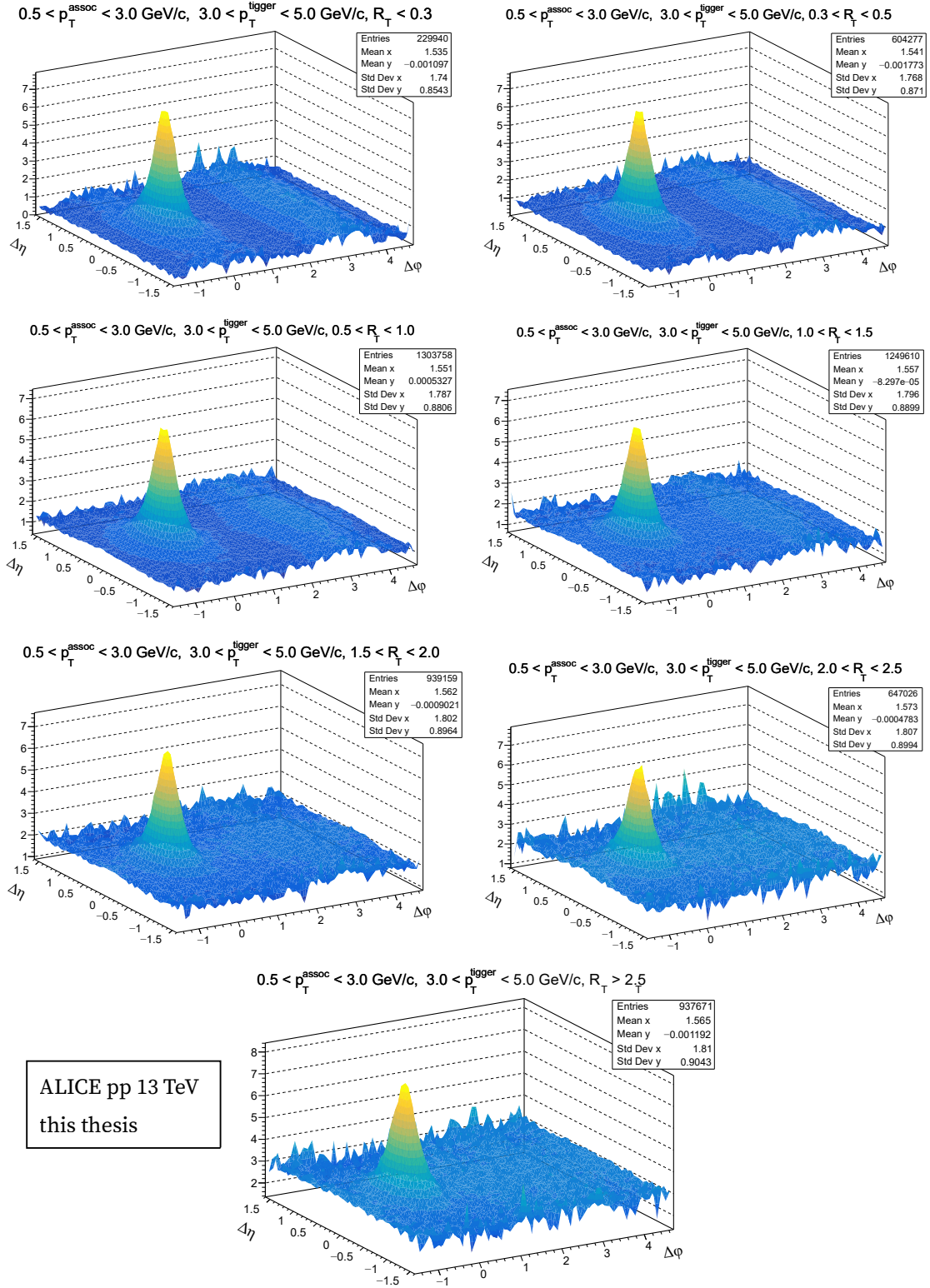
Figure 25: *Configuration 1*: Per-trigger correlation functions in $(\Delta\eta,\ \Delta\varphi)$ for different R_T, for the mid transverse momentum bin $(1.0 < p_T^{assoc} < 3.0 \text{ GeV/c})$.

Figure 26: *Configuration 1*: Per-trigger correlation functions in $(\Delta\eta, \Delta\varphi)$ for different R_T, for the highest transverse momentum bin $(3.0 < p_T^{assoc} < 5.0 \text{ GeV/c})$.
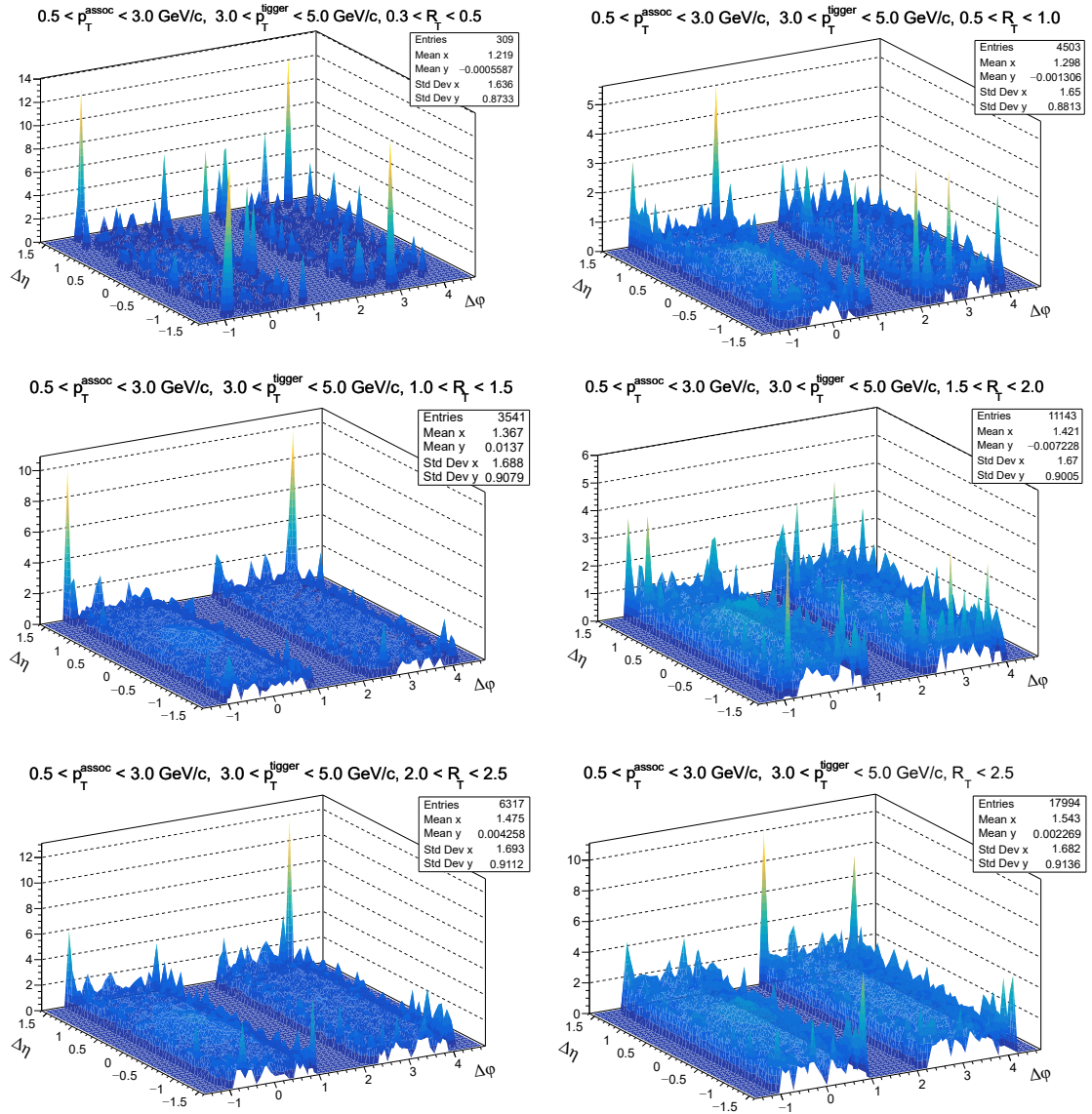
Figure 27: *Configuration 2*: Per-trigger correlation functions in $(\Delta\eta,\ \Delta\varphi)$ for different R_T, for the only transverse momentum bin $(0.5 < p_T^{assoc} < 3.0$ GeV/c).

Figure 28: *Configuration 3*: Per-trigger correlation functions in $(\Delta\eta, \Delta\varphi)$ for different R_T, in the transverse region.
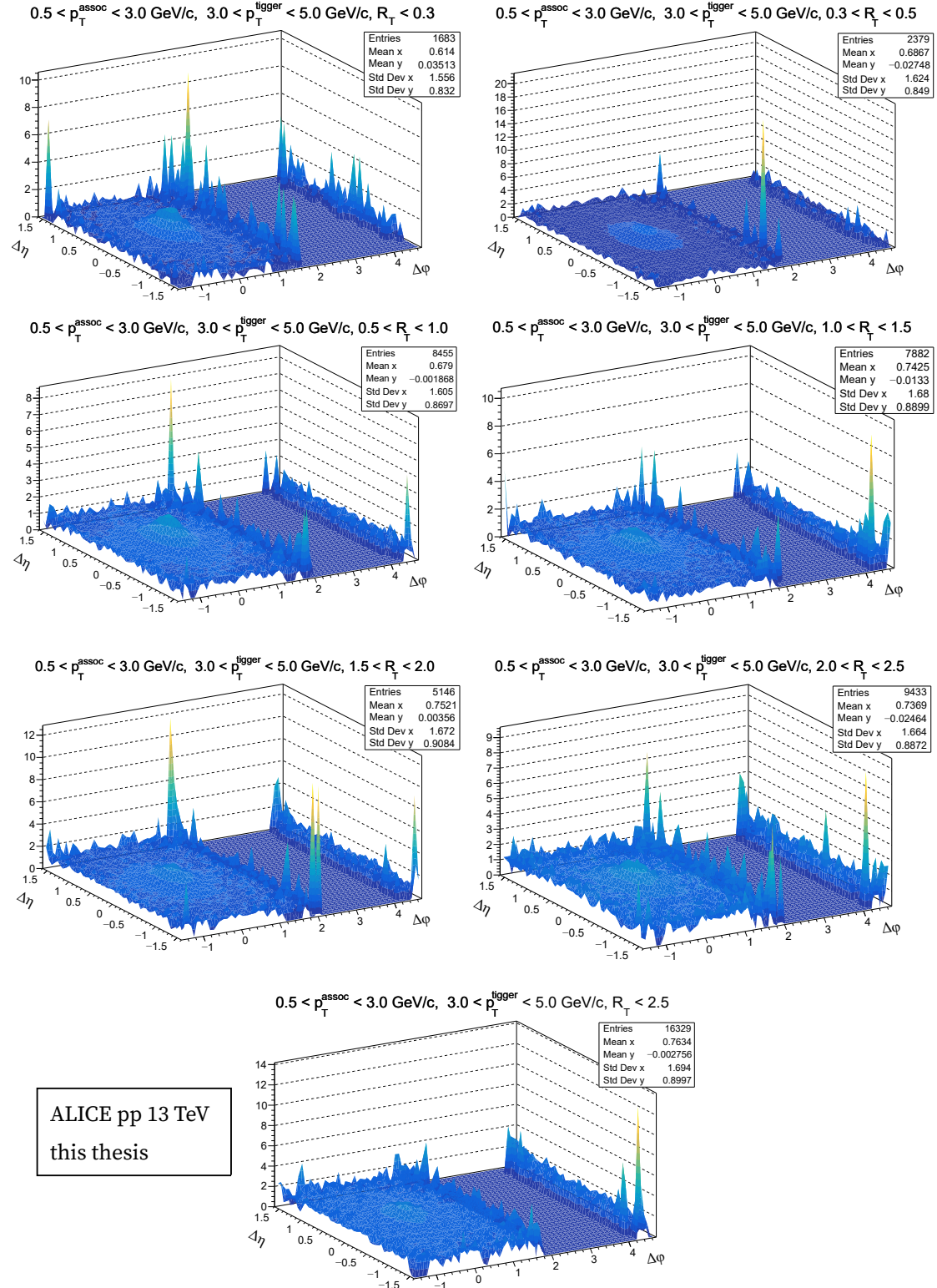
Figure 29: *Configuration 3*: Per-trigger correlation functions in $(\Delta\eta, \Delta\varphi)$ for different R_T, in the toward region.
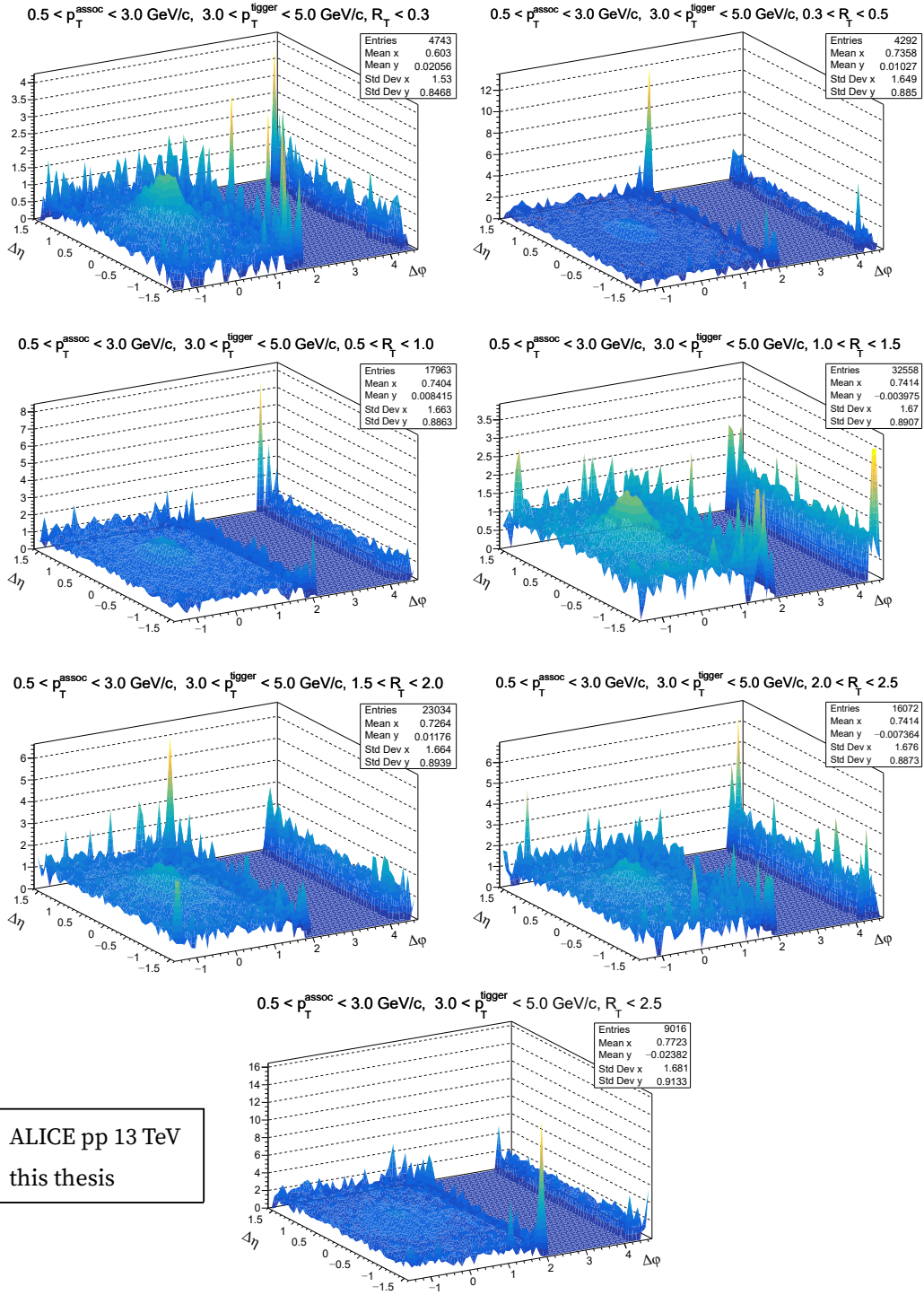
Figure 30: *Configuration 3*: Per-trigger correlation functions in $(\Delta\eta, \Delta\varphi)$ for different R_T, in the away region.